Analytical Corrections of Banding Artifacts in Driven Equilibrium Single Pulse Observation of T2 (DESPOT2)

Jean-David Jutras[1], Keith Wachowicz[1,2], Nicola De Zanche[1,2,*]

1. Department of Oncology, University of Alberta, Edmonton, Alberta, Canada
2. Department of Medical Physics, Cross Cancer Institute, Edmonton, Alberta, Canada

Published in
Magnetic Resonance in Medicine
DOI: 10.1002/mrm.26074

***Corresponding author:**
Nicola De Zanche
Department of Medical Physics
Cross Cancer Institute
11560 University Avenue
Edmonton, Alberta, Canada
T6G 1Z2

Telephone: 780-989-8155
Fax: 780-432-8615
Email: dezanche@ualberta.ca

ABSTRACT

Purpose

DESPOT2 is a single-component T_2 mapping technique based on bSSFP imaging. It has seen limited application because of banding artifacts and magnetization transfer (MT) effects. In this work, acquisitions are optimized to minimize MT effects, while exact and approximate analytical equations enable automatic correction of banding artifacts within the T_2 maps in mere seconds.

Methods

The technique was verified on an agar phantom at 3T. The T_2 resulting from four different data combination techniques was compared to the T_2 from CPMG. Two comparable DESPOT2 scan protocols (short vs. long TR/T_{RF}) designed to minimize MT effects, were tested both in the phantom and in vivo. A third protocol was tested in the brain of 8 volunteers and analytical correction schemes were compared with DESPOT2-FM.

Results

The T_2 measurements in agar agree with CPMG within ~7% and in-vivo protocol results agree with values reported in the literature. The approximate analytical solutions provide increased robustness to hardware imperfections and higher T_2-to-noise ratio than the exact solutions.

Conclusions

New analytical solutions enable fast and accurate whole-brain T_2 mapping from bSSFP images with a minimum of two phase offsets and two flip angles (=4 datasets, 8 min scan) and previously measured T_1 and B_1 maps.

Introduction

Quantitative mapping of the T_1 and T_2 relaxation constants in vivo can provide improved sensitivity to biochemical changes in tissues associated with disease over conventional T_1-weighted and T_2-weighted MRI (1), (2), (3). The methods of Variable Flip Angles (VFA) or Driven Equilibrium Single Pulse Observation of T_1 (DESPOT1) for fast 3D T_1 mapping have gained popularity in recent years in applications such as brain and knee imaging (4), (5), (6), (7), by virtue of their simplicity and excellent signal-to-noise ratio (SNR) efficiency. In these methods, two or more spoiled gradient recalled echo (SPGR) datasets are acquired at different flip angles and the T_1 is extracted from the slope of a linear fit of the SPGR signal. Advances in transmit B_1/flip-angle mapping have made the implementation of DESPOT1 practical at 3T (8), (9), (10), where the effect of transmit B_1 inhomogeneity is more severe than at 1.5 T and must be corrected.

Conversely, the DESPOT2 method for mapping T_2 has not achieved similar success because it relies on balanced steady state free precession (bSSFP) which is prone to banding artifacts that arise from off-resonance (ΔB_0), corrupting the T_2 map (11), (12). More recently, magnetization transfer (MT) and finite RF pulse effects were also shown to bias the resulting T_2 (13), (14). Consequently, T_2 mapping continues to rely on spin-echo based techniques such as dual-echo or multi-echo fast-spin echo sequences (15), (16), which, however, cannot provide whole-brain T_2 maps with high isotropic resolution (~1 mm) in a reasonable scan time. Deoni et al. proposed the "phase-cycled DESPOT2" (DESPOT2-c) (12) and "DESPOT2 with full modeling" (DESPOT2-FM) (17) techniques to address the problem of banding artifacts. Unfortunately, both approaches utilize computationally-intensive post-processing algorithms and significantly longer post-processing time than the original DESPOT1/DESPOT2 methods. (DESPOT2-FM processing may take up to 48 hours for a single 1-mm isotropic 3D brain dataset, when running on a single-core CPU (18)). Furthermore, both methods are limited to two phase cycles, while using a larger number improves the robustness of the results. The method of Wood et al. (18) removes band artifacts in DESPOT2 using the "geometric solution" for bSSFP imaging (19) and is valid for exactly four phase offsets.

In this study, we remove banding artefacts analytically by introducing the *reduced* T_2 from DESPOT2 and performing a general mathematical analysis that includes the effect of off-

resonance and is valid for any number of phase cycles greater than one. Using an even number of phase offsets, an exact mathematical solution is derived to obtain both T_2 and phase accumulation, ϕ, with computational ease. Moreover, we show that with three or more phase offsets, an approximate but accurate solution for T_2 can also be used. We finally investigate two approaches for mitigating MT effects that otherwise bias the T_2 measurement: optimization of the flip angles/ RF pulse durations to cancel the MT ratios (MTR), and lengthening the RF pulse durations. All methods are readily applied with minimal sequence development on any modern clinical scanner on which bSSFP, SPGR and B_1^+ mapping sequences are implemented.

Theory

Solving for T_2 Analytically

The full bSSFP signal in steady-state is given by Zur et al. (20), (21)

$$M_+ = \frac{a\, e^{-i(\phi+\phi_{RF})} + b}{c\cos(\phi+\phi_{RF}) + d} M_0\, e^{-TE/T_2}, \qquad (1)$$

$$a = -(1-E_1)\sin\alpha\, E_2, \quad b = (1-E_1)\sin\alpha, \quad c = E_2(E_1-1)(1+\cos\alpha), \quad d = 1 - E_1\cos\alpha - E_2^2(E_1-\cos\alpha),$$

where, $\phi = 2\pi\, \Delta f\, TR$ is the phase accumulation arising from the static field inhomogeneity and chemical shift, $\Delta f = \gamma(1+\sigma)B(\bar{r})/2\pi - f_0$, TR is the repetition time, σ is the chemical shift constant, and ϕ_{RF} is the RF phase cycle increment. Furthermore $E_1=exp(-TR/T_1)$, $E_2=exp(-TR/T_2)$, TE is the echo time, α is the actual flip angle, and $M_+=M_x+iM_y$ is the transverse magnetization.

When the signal is perfectly on resonance (Δf=0) and the phase cycle is $\phi_{RF}=\pi$, Eq. (1) simplifies to

$$S_{SSFP} = M_0 \frac{(1-E_1)\sin\alpha\, e^{-TE/T_2}}{1-(E_1-E_2)\cos\alpha - E_1E_2}, \qquad (2)$$

i.e., $S_{SSFP} = |M_+|$, which is the better-known equation that describes the magnitude of the bSSFP signal. In the DESPOT2 technique, multiple bSSFP datasets are acquired at respectively different flip angles, while keeping all other scan parameters identical. These datasets are then curve-fitted using a linearized (y=m x + b) version of Eq. (2), given by (5)

$$\frac{S_{SSFP}}{\sin\alpha} = \frac{E_1 - E_2}{1 - E_1 E_2}\frac{S_{SSFP}}{\tan\alpha} + \frac{M_0(1-E_1)e^{-TE/T_2}}{1 - E_1 E_2}, \quad (3)$$

where $y=S_{SSFP}/\sin\alpha$, $x=S_{SSFP}/\tan\alpha$, the slope $m=(E_1-E_2)/(1-E_1E_2)$, and the intercept $b=M_0(1-E_1)e^{-TE/T2}/(1-E_1E_2)$. Expressions and results for the proton density M_0 in the presence of banding artefacts are provided in the online supporting information.

The T_2 can be determined from the slope m, the TR, and the T_1 previously determined from a technique such as DESPOT1 (5). In practice, however, off-resonance will result in a systematic underestimation of T_2, that we define "reduced T_2"

$$\tau_2(\phi) = -TR / \log\left(\frac{E_1 - m(\phi)}{1 - m(\phi)E_1}\right) \le T_2, \quad (4)$$

where $m(\phi)$ shows explicitly that the measured slope is modulated by the off-resonance phase ϕ. The relationship between τ_2 and T_2 is derived in Appendix A, resulting in a simple function of ϕ and T_2, notably independent of T_1,

$$\tau_2(\phi) = -TR / \log\left(\frac{e^{-TR/T_2} + \cos\phi}{e^{TR/T_2} + \cos\phi}\right). \quad (5)$$

To demonstrate the periodic nature of the banding artifacts in both the bSSFP signal and τ_2, Eq. (1) is plotted in Figure 1(a), as a function of α and ϕ, (with T_1=1000ms, T_2=70ms, TE=2.3 ms, TR=4.6 ms), along with Eq. (5) normalized by the true T_2 in Figure 1(b) as a function of $t=TR/T_2$ and ϕ. At low flip angles, the bSSFP signal can suffer from either bright-band or dark-band artifacts, while at high flip angles, the signal suffers from dark-band artifacts (22). Conversely, τ_2 suffers from systematic underestimation and actually becomes complex when $E_1 - m < 0$. This region, corresponding to areas near off-resonance in Figure 1b), tends to vanish for very long T_2, as $t \to 0$. The practical consequences arise in the presence of noise, and the effects in the final T_2 map can be minimized as described at the end of this section.

Banding artifacts are generally dealt with by acquiring bSSFP datasets at different phase offsets by either changing the RF phase cycle increment ϕ_{RF}, or changing the transmit frequency f_{tr} (since they have an equivalent effect on Eq. (1)). The total phase offset resulting from ϕ_{RF} or Δf_{tr} is defined as $\theta = 2\pi TR\Delta f_{tr} + \phi_{RF} - \pi$. Various methods for synthesizing artifact-free bSSFP images from different phase-cycled datasets have been developed and their performance has been compared (22), (23). Generally, the quality of the synthesized image improves with an increasing

number of phase offsets and for best results, the number of phase offsets must be evenly distributed over a full period. The phase offset θ corresponds to a frequency offset of (21)

$$\Delta f_0 = \frac{\theta}{2\pi TR}. \tag{6}$$

Multiple bSSFP datasets are acquired with several (N) phase offsets (i.e., θ_1, θ_2,... θ_N), each with two different flip angles α_1, α_2 (totalling $2N$ datasets). For each offset θ_i, one τ_2 map is obtained from the measured slope (from magnitude signals x and y defined below Eq.(3)) by substituting

$$m^{\theta}(\phi) = \frac{y_1 - y_2}{x_1 - x_2} = \frac{S^{\theta}_{SSFP}(\alpha_1)/\sin\alpha_1 - S^{\theta}_{SSFP}(\alpha_2)/\sin\alpha_2}{S^{\theta}_{SSFP}(\alpha_1)/\tan\alpha_1 - S^{\theta}_{SSFP}(\alpha_2)/\tan\alpha_2}, \tag{7}$$

into Eq. (4). A method of reducing the effect of the bands in the final T_2 maps is to simply take the maximum intensity projection (MIP) of two τ_2 maps (12). However, a systematic underestimation of the true T_2 will still remain at locations where the off-resonance lies between the two offsets. Fortunately, the derivation of Eq. (5) leads to an exact solution. Rearranging Eq. (5), we may write

$$E_2^2 - E_2(1-\varepsilon_2^{\theta})\cos(\phi+\theta) - \varepsilon_2^{\theta} = 0, \text{ where} \tag{8a,b}$$

$$\varepsilon_2^{\theta} = e^{-TR/\tau_2(\phi+\theta)}.$$

Note that $\varepsilon_2^{\theta} \in [-1,1]$ and Eq. (8b) is valid for both real and complex values of τ_2. Because $\cos(\phi+\pi) = -\cos(\phi)$, with two phase offsets $\theta = 0, \pi$ we have a system of two non-linear equations and two unknowns (T_2 and ϕ), the solution of which is (Appendix B):

$$T_2^{0,\pi} = -TR \Big/ \log\left(\sqrt{\frac{2\varepsilon_2^0\varepsilon_2^{\pi} - \varepsilon_2^0 - \varepsilon_2^{\pi}}{\varepsilon_2^0 + \varepsilon_2^{\pi} - 2}}\right) \tag{9 a, b}$$

$$\cos\phi^{0,\pi} = \frac{\varepsilon_2^0 - \varepsilon_2^{\pi}}{\sqrt{(\varepsilon_2^0 + \varepsilon_2^{\pi} - 2)(2\varepsilon_2^0\varepsilon_2^{\pi} - \varepsilon_2^0 - \varepsilon_2^{\pi})}}.$$

The 0, π superscript on T_2 indicates the phase offsets used. A more general form of these equations shown in Appendix B is actually valid for any pair of offsets having opposite phase, thus allowing additional estimates of T_2 to be calculated by sampling 0–2π using other pairs of offsets with opposite phases. These T_2 maps can then be combined by weighted average with

optimal weights given by the square of the sine or cosine of the off-resonance phase ϕ. For example, with four phase offsets the final T_2 is

$$T_2 = \frac{\sin^2(\phi^{\pi/2,3\pi/2})\, T_2^{0,\pi} + \cos^2(\phi^{0,\pi})\, T_2^{\pi/2,3\pi/2}}{\sin^2(\phi^{\pi/2,3\pi/2}) + \cos^2(\phi^{0,\pi})}, \tag{10}$$

which we define as the "exact weighted" solution for $N=4$. A simple closed-form solution does not exist for odd numbers of phase offsets (e.g., θ=0, 2π/3, 4π/3). In this case it is more practical to employ a root-sum-of-squares combination (RSS):

$$T_2 \cong K_N \sqrt{\sum_{n=1}^{N} \left(\tau_2^{\theta_n}\right)^2}\ ,\ N \geq 3\,. \tag{11}$$

This approximate solution for deriving a final T_2 map is based on the assumption that $TR<<T_2$. Thus the shorter the TR, the more accurate is the approximation. The factor K_N is calculated by substituting Eq. (5) into Eq. (11) and taking the limit as $t=TR/T_2 \rightarrow 0$. It can be proven by mathematical induction that for any (even or odd) N phase offsets $K_N = \sqrt{8/3N}$. Note that if using only two phase offsets this RSS combination will fail to yield an accurate final T_2 map, (because the limit depends on ϕ) and Eq. (9) must be used instead.

The final RSS approximation is,

$$T_2 \cong \sqrt{\frac{8}{3N}}\, TR \sqrt{\sum_{n=1}^{N} \left[\log\left(\frac{e^{-t} + \cos(\phi + \theta_n)}{e^{t} + \cos(\phi + \theta_n)}\right)\right]^{-2}}\ . \tag{12}$$

Equation (12) is plotted in Figure 1(c), and (d) for N=3 and 4, respectively, by normalizing the calculated T_2 by the actual T_2 (as shown for a single phase offset in Figure 1b). The proposed RSS solution introduces negligible errors (maximum ~5% for N = 3 at $T_2=TR$). A flowchart of the analytical DESPOT2 post-processing pipeline is shown in Figure 2. Note that T_1 is also needed, along with the B_1 inhomogeneity correction c_{RF}^{+} map (defined as actual flip angle α divided by the nominal flip angle α_n) from a B_1-mapping sequence, such as Actual Flip Angle Imaging (AFI) (8).

Finally, while Eq. (9) is exact for both positive and negative ε_2 (real and complex τ_2, respectively), in practice $\varepsilon_2<0$ identifies regions near the off-resonance condition where signal is low and noise becomes significant. Also, here the bSSFP signal is sensitive to hardware imperfections (such as eddy currents, or frequency drifts) because of the presence of unstable

equilibrium (24). In these locations more reliable data from other offsets must carry a larger weight to ensure a reliable estimate for T_2. One way to achieve this is to assign values for $\varepsilon_2^\theta \in$ [-1, 0] in Eq. (9) for the exact solution or to exclude that datum from the RSS combination by assigning τ_2^θ=0 in Eq. (11) wherever $E_1\text{-}m^\theta \leq 0$. We have chosen $\varepsilon_2^\theta = 0$ in Eq. (9), but with prior knowledge of the expected values of T_2 other ε_2^θ values may be chosen (e.g., ε_2^θ=–0.45, if T_2~50 ms) to minimize potential bias. We must also assign these values to voxels where $|\varepsilon_2^\theta| > 1$, which can only occur in noise-dominated regions (i.e. $E_1\text{-}m^\theta \leq 0$).

<Figure 1>

<Figure 2>

Effect of Finite RF Pulses and Magnetization Transfer on T_2

Recently, Bieri et al. have demonstrated that in vivo bSSFP is prone to on-resonance magnetization transfer (MT) effects, especially at short *TR* and high flip angles (25). Moreover, the actual bSSFP signal may deviate considerably from that of Eqs. (1) and (2) due to the finite length of RF pulses (See Figure 3a). Consequently, DESPOT2 may yield incorrect white matter (WM) and gray matter (GM) T_2.

Finite RF pulse effects can be accounted for in Eq. (2) by the following substitution (26):

$$E_2 \rightarrow \widetilde{E}_2 = \exp(-(TR - \zeta_\phi T_{RF})/T_2), \tag{13}$$

$$\zeta_\phi = \zeta \cos^2\left[\frac{\phi}{2}\left(1-(1-\zeta)\frac{T_{RF}}{TR}\right)\right], \quad (\text{for } 2\,|\alpha/\phi| > T_{RF}/TR), \tag{14a}$$

$$\zeta \approx 0.68 - 0.125\left(1+\frac{T_{RF}}{TR}\right)\frac{T_2}{T_1}, \tag{14b}$$

where T_{RF} is the RF pulse duration (for hard pulses). To avoid MT effects, Crooijmans et al. suggest using a combination of longer *TR* and T_{RF} (13), and a correction for the finite T_{RF} based on Eqs. (15, 16 and 20) of Ref. (26). These corrections are exact only on-resonance, and the above DESPOT2 solutions Eqs. (9)– ((10) are only valid in the limit of negligible RF pulse durations (e.g., $T_{RF}/TR \leq 0.15$). As shown in Figure 3b (blue curve), finite RF pulse effects will bias the calculated T_2 to longer values, as well as introducing oscillations. While the simple substitution $TR \rightarrow TR_{eff} = TR - \zeta_{corr} T_{RF}$ can be made in Eq. (4) or (9) to correct the net bias, the oscillations cannot be fully removed, even if using the phase information in Eq. (14a). While the

finite RF pulse correction of Eqs. (13) and (14) is strictly valid only for $T_{RF1}=T_{RF2}=T_{RF}$ (26) we may use $T_{RF}=T_{RF2}$, since as shown in Figure 3(a), T_{RF2} dominates on both the SSFP signal bias at α_2 and the resulting T_2 bias. (The effect is also well illustrated using Bloch simulations in Fig. 2 of Ref. (14).)

There are two straightforward ways to mitigate MT effects. The first option is to significantly stretch both T_{RF1}/T_{RF2}, and increase the TR in an attempt to essentially remove the MT effects from both bSSFP signals at α_1/α_2. The main disadvantage of this approach is that stretching the RF pulses will lead to spatial spectral effects (i.e., the edges of the brain and adipose/fat tissue may no longer be properly excited (26)), and the final corrected T_2 map will contain more oscillations.

The second option (13) is to still use a short TR (~4–5 ms) and short T_{RF} (<0.7 ms), but also to select two flip angles (α_1 and α_2) such that the MT ratio (MTR) of the bSSFP signal at α_1 will be approximately equal to the MTR at α_2 in WM (or a compromise between WM and GM). This will result in the MTR cancelling out when calculating the slope in Eq. (3), and yield a good approximation for τ_2. This method was initially proposed with flip angles α_1/α_2=25/80˚ (assuming a short TR, and equal T_{RF} for both lower and higher flip angles) (13). However, this choice yields a significantly suboptimal T_2NR in WM or GM, because the two flip angles are not the optimal values (optimal T_2NR is achieved with α_1/α_2≈11/57°, assuming WM T_1/T_2≈1000/52 or GM T_1/T_2≈1400/75 ms using Eq. 12 in Ref. (5)).

A better alternative that maintains the T_2NR efficiency is to let the scanner software freely adjust the T_{RF} for any given α, (to avoid exceeding maximum allowable SAR as done in Ref. (27)) and then select the lower and higher flip angles ($\alpha_1 < \alpha_2$), such that they simultaneously experience the same amount of MT, while remaining close to their SNR-optimal values. As shown in the online Supporting Figure S1, in vivo MTR measurements were performed in the brain of a healthy volunteer using bSSFP images acquired in flip angle increments of 5° over a range of 5–85° (Figure S1(c)), obtained similarly to Gloor et al. (28). The measured signal is curve-fitted assuming the on-resonance two-pool bSSFP equation (which accounts for MT effects) to solve for T_2, M_0, and the exchange parameters k_f and F, given the known input scan parameters (α, T_{RF}, $\omega_1(t)$, TR, TE) and the T_1 from DESPOT1(28). The theoretical single-pool bSSFP signal is then obtained (see Figure S1(a) and (b)) by substituting the measured T_1, T_2 and M_0 into Eq. (2). Finally, the MTR is calculated as the percent difference between the single-pool and the two-

pool bSSFP signals. The flip angles at which the MT effects are equal are found visually (Figure S1(c)) to be approximately α_1/α_2=11.5±1/59±2° with corresponding T_{RF1}/T_{RF2}=0.064/0.55 ms, and TR=4.8 ms. This choice simultaneously minimizes MT effects while optimizing the T2NR efficiency defined as the T2NR divided by the square-root of the scan time (5).

Effect of Image Noise on T_2

It is important to study how noise in both the T_1 map and in the bSSFP datasets propagates into the final T_2 map, as well as how to choose phase offsets, flip angles, and/or the number of averages (NEXs) to maximize the T2NR efficiency. Deoni et al. have shown that taking multiple averages at two optimized flip angles yields a higher T2NR (at a reference T_2) than curve-fitting multiple datasets of varying flip angles (5). They also found that the optimal examination protocol dedicates 75% of the total scan time to DESPOT1 and the remaining 25% to DESPOT2. However, this analysis assumes a perfect on-resonance condition with only one phase offset (θ=0). We now investigate how noise will propagate into the final T_2 map, when 2, 3 or 4 phase offsets are used (Eqs.(9), ((10), or ((11)), including off-resonance effects while ignoring finite RF pulse effects.

In the simplest case of two on-resonance bSSFP datasets S_1 and S_2 with respective flip angles α_1, α_2, and a T_1 map previously derived from DESPOT1, the noise standard deviation σ_2 in the final T_2 may be calculated by standard error propagation (assuming the SNR is sufficiently high and uncorrelated Gaussian noise)

$$\sigma_2 = \sqrt{\left(\frac{\partial T_2}{\partial S_1}\right)^2 \sigma_s^2 + \left(\frac{\partial T_2}{\partial S_2}\right)^2 \sigma_s^2 + \left(\frac{\partial T_2}{\partial T_1}\right)^2 \sigma_1^2}\,, \tag{15}$$

where σ_s is the noise standard deviation in either bSSFP dataset and σ_1 is the noise standard deviation in the T_1 map. The final result (see Appendix C) is

$$\sigma_2 = \sqrt{\frac{T_2^4(1-E_1E_2)^2}{TR^2}\frac{(1-E_1E_2+(E_2-E_1)\cos\alpha_1)^2\csc^2\alpha_1 + (1-E_1E_2+(E_2-E_1)\cos\alpha_2)^2\csc^2\alpha_2}{E_2^2(1-E_1^2)^2(S_1\cot\alpha_1 - S_2\cot\alpha_2)^2}\sigma_s^2 + \frac{E_1^2(1-E_2^2)^2T_2^4}{E_2^2(1-E_1^2)^2T_1^4}\sigma_1^2}$$

(16).

In off-resonant conditions the standard deviation for τ_2 can be obtained by substituting the T_2 for τ_2 from Eq. (5) into Eq.(16), resulting in

$$\sigma_2(\phi)=\sqrt{\frac{\tau_2(\phi)^4(1-E_1\varepsilon_2(\phi))^2}{TR^2}\frac{(1-E_1\varepsilon_2(\phi)+(\varepsilon_2(\phi)-E_1)\cos\alpha_1)^2\csc^2\alpha_1+(1-E_1\varepsilon_2(\phi)+(\varepsilon_2(\phi)-E_1)\cos\alpha_2)^2\csc^2\alpha_2}{\varepsilon_2(\phi)^2(1-E_1^2)^2(S_1(\phi)\cot\alpha_1-S_2(\phi)\cot\alpha_2)^2}\sigma_s^2+\frac{E_1^2(1-\varepsilon_2(\phi)^2)^2\tau_2(\phi)^4}{\varepsilon_2(\phi)^2(1-E_1^2)^2T_1^4}\sigma_1^2}$$

(17).

To find the T2NR in the analytical solution Eq. (9a), we must calculate

$$\sigma_2^{0,\pi}(\phi)=\sqrt{\left(\frac{\partial T_2^{0,\pi}}{\partial\tau_2^0}\right)^2\sigma_2^0(\phi)^2+\left(\frac{\partial T_2^{0,\pi}}{\partial\tau_2^\pi}\right)^2\sigma_2^\pi(\phi)^2}\,, \tag{18}$$

where $T_2^{0,\pi}$ and τ_2^θ are previously defined. A similar equation applies for $\sigma_2^{\pi/2,3\pi/2}(\phi)$. The final result is not algebraically concise but clearly predicts that T2NR is a periodic function of ϕ as plotted in Figure 2(c).

Performing the same error analysis on the approximate solution for T_2 given in Eq. (11), we obtain

$$\sigma_2^{RSS}(\phi)=\sqrt{\frac{8}{3N}}\frac{\sqrt{\sum_{n=1}^{N}\left(\tau_2^{\theta_n}\right)^2\left(\sigma_2^{\theta_n}\right)^2}}{\sqrt{\sum_{n=1}^{N}\left(\tau_2^{\theta_n}\right)^2}}. \tag{19}$$

This T_2 noise standard deviation is much more uniform with respect to ϕ than that of the exact solution calculated in Eq. (18) as shown in Figure 3(c). Note how the RSS combination of the reduced T_2 yields a more uniform T2NR than the exact, or exact weighted analytical solutions. In fact, spikes (arising from noise in the vicinity of the singularity where E_1-$1\leq 0$) occur at regular intervals of $\phi=n\pi$ in the exact solution derived from two phase offsets ($\theta = 0, \pi$), resulting in a highly non-uniform T2NR (red curve). Using the exact weighted solution with four different phase offsets (N=4, magenta curve), and weighing the analytical T_2 by the squared sine or cosine of the phase as done in Eq. (10) eliminates the spikes. The T2NR derived analytically is also verified by a Monte Carlo-based T2NR simulation from MATLAB in the online Supporting Figure S2.

<Figure 3>

Methods

Phantom Measurements

Because banding artifacts are more easily identified in uniform gel phantoms than in vivo, DESPOT2 was first optimized on a phantom prior to being tested on volunteers. The phantom was built by pouring 7 different layers of agar solutions (7g/L) doped with varying concentrations of $MnCl_2$ (0–400 μM) into a plastic container (dimensions: $12\times12\times20$ cm^3). Each layer was allowed to harden, then covered with cellophane wrap before pouring the next layer to prevent diffusion. The phantom was scanned on a 3T Philips Achieva scanner with an 8-channel head array, and T_1 maps were obtained using the DESPOT1 technique (scan time: 5 min per dataset) (5), utilizing a multi-echo SPGR acquisition. Flip angle non-uniformity was acquired using an Actual Flip Angle Imaging (AFI) sequence (scan time: 3 min) (8). First-order shimming was performed automatically by the scanner as part of the preparation phase.

Two optimized DESPOT2 protocols were tested, each containing 2 flip angles by 4 phase offsets (= 8 datasets, scan time: ~2 min per dataset). The first protocol (bSSFP1) had short TR/T_{RF}, high bandwidths (517 Hz/pix) and flip angles (α_1/α_2=12/58°) chosen to cancel the MT effects in WM/GM as previously explained in the Theory. The second protocol (bSSFP2) was devised to minimize the MT effects by employing long TR/T_{RF}, and lower flip angles (α_1/α_2=*9/35*°). The bandwidth was decreased, and parallel imaging (regularized SENSE (29)) acceleration increased to yield approximately the same SNR efficiency and scan time as the first protocol. Note that the phase offsets (θ = 0, π/2, π, 3π/2) were achieved by changing the transmit frequency f_{tr} according to Eq. (6), rather than by changing the phase-cycling scheme, and all RF pulses were non-selective. We found that changing the transmit frequency yields more accurate T_2 maps than changing the phase-cycling scheme because slow drifts in the Larmor frequency can be compensated for by automatic transmit frequency recalibration during the preparation phase of each scan.

To verify the accuracy of T_2, the phantom was also scanned with a 32-echo CPMG sequence to obtain comparative T_2 values in a 2D axial slice at the centre of the phantom. The T_2 values were obtained by fitting using the StimFit 1.0 MATLAB toolbox (http://mrel.usc.edu/). This method assumes single-component mono-exponential T_2 decay and uses extended phase graph (EPG) simulation to correct for both stimulated echoes and B_1 inhomogeneity effects (30). An additional DESPOT2 experiment (bSSFP0) was also tested with parameters designed to

minimize the effect of finite RF pulses. All pulse sequences tested on the phantom and their respective scan parameters are listed in Table 1.

All datasets were reconstructed and zero-padded to 3D image matrices of 256×256×180 in MATLAB using the ReconFrame package (Gyrotools, LLC, Switzerland). T_2 and ϕ maps were calculated using both the exact analytical solutions of Eqs. (9)– ((10) and the RSS solution of Eq. (11) as summarized in the flowchart of Figure 2. A correction for finite RF pulse duration was also applied using the substitution $TR \rightarrow TR_{eff} = TR - \zeta_{corr} T_{RF}$ in Eq. (9) with ζ_{corr}=0.498 for the exact solution (with N even) and in Eq. (4) with ζ_{corr}=0.555 for the RSS solution (with N=3 or 4) as done similarly by Crooijmans and Bieri for N=1 (14), (26). The T_2 was measured in 3D ROIs of 21×21×5 pixels at both a central and an off-centre location of each layer.

Performance of the proposed analytical corrections was compared with the DESPOT2-FM technique by implementing the stochastic region contraction (SRC) algorithm in MATLAB, and using the same parameters N_1=5000, N_2=25, and initial search space $0 \leq T_2 \leq 500$ ms and $0 \leq \phi \leq 2\pi$, described in Ref. (17). Note that DESPOT2-FM is also governed by Eq. (1) and thus does not account for finite RF pulse duration and MT effects. Additionally, M_0 was also allowed to vary freely as an optimization parameter, rather than factored out by normalizing the data (17). On average, SRC converged in 4–7 iterations, and took ~19 ms per voxel. Finally, equations (13)–(14c) were used to correct the resulting T_2 for finite RF pulse effects, as described in Ref. (27).

<Table 1>

In vivo Measurements

Informed consent was obtained and a healthy 30 year-old male volunteer was scanned using the same DESPOT1 and DESPOT2 protocols used on the phantom (Table 1). Eight volunteers (4 males and 4 females aged 21–30 years) were also scanned as part of a reduced examination protocol of ~27 min duration, comprising the same AFI sequence as in Table 1, but with different SPGR (T_{scan}~12 min) and bSSFP (T_{scan}~12 min) scan parameters, denoted as SPGRb, and bSSFP3. For each subject, the T_2 (calculated using the approximate RSS solution with N=3), the T_1 and the T_2^* were measured in ROIs of different brain regions, with and without the correction for finite RF pulse duration. The global mean T_2 was also measured in 4 different tissue classes (GM, WM, adipose, and muscle) by segmenting the brain using thresholds based on the T_1 histogram (31). Note that one of the volunteers was the same subject (v2) for which the

protocols in Table 1 were tested, thus enabling further comparisons to be made between the bSSFP1 and bSSFP2 protocols. For this volunteer, 2D spin-echo (SE) images were also acquired (same transverse slice location as the CPMG) with the following parameters: FOV=170×240 mm^2, resolution=1.2×1.2×5 mm, TE=15, 30, 45, 60, 75 and 105 ms, TR=1500 ms, scan time=3:30 min per image). Images acquired at varying TEs were least-squares fitted pixelwise to a mono-exponential to obtain another T_2 map. For this volunteer SRC fitting was also performed on both bSSFP1 and bSSFP2 data using the same initial conditions as for the phantom.

Each in-vivo 3D dataset was exported into 3D slicer (32) and co-registered to correct mismatches arising from slight head motion during the examination. Curve-fitting in MATLAB takes only ~20 s per subject (excluding the image reconstruction time) on a PC with an Intel Core i7-3770 CPU and 32GB of RAM.

Results

Phantom Measurements

Phantom bSSFP images and profiles of the calculated T_2 are shown in Figure 4 for the DESPOT2 protocol with the longer TR=9.2 ms, and short T_{RF2}=0.28 ms. The resulting T_2 is compared to that of the protocol with a longer T_{RF2}=2.0 ms. As predicted by the theory, stretching the RF pulse duration leads to more significant oscillations in the final T_2 (dashed black curve). Moreover, since the measured B_1 field homogeneity is altered by the spatial-spectral effects of the long T_{RF}, the T_2 calculated from bSSFP2 with TR/T_{RF2}=9.0/2.0 ms is systematically underestimated at the edges of the phantom (Figure 4d).

<**Figure 4**>

Sagittal slices of the τ_2 maps are shown in Figure 5, along with the T_2 calculated with the exact solution of Eq. (9), the exact weighted solution of Eq. (10), the RSS solution of Eq. (11), and SRC fitting technique, for both DESPOT2 protocols. A profile through a single layer (red line) is also plotted in the bottom row to visualize the differences between the analytical methods and the SRC-based T_2 fits. At short T_{RF2}=*0.55* ms (bSSFP1), and N=*2*, SRC shows fewer oscillations than the analytical methods. However, with N=*4*, these differences disappear. At long T_{RF2}=2 ms (bSSFP1), all methods exhibit oscillations, and the RSS solution performs best as predicted in Figure 3d. The finite RF pulse correction applied following SRC at long T_{RF2}=2.0 ms also

appears to over-correct T_2, as visible in the profiles. Furthermore, the T_2 from SRC oscillates between large over- and under-estimation in regions of spatial-spectral effects (green arrows), while the analytical solution yields a gradual under-estimation in T_2. The percent difference between the exact-weighted T_2 solution and the RSS solution with $N=4$ is also shown as colored intensity in both Figure 5(a) and (b). Differences range within ±3% for short T_{RF2} in (a) and ±6% for long T_{RF2} in (b), with the RSS solution exhibiting fewer oscillations.

The cosine or sine of the phase maps calculated from Eq. (9b) are displayed in Supporting Figure S3 for both DESPOT2 protocols. The arrows indicate minor discontinuities within the phase, caused by slight mismatches in the locations of the bands across the different bSSFP datasets (also leading to a spike or edge in the T_2 (red arrow in Figure 5a)) that are attributed to hardware imperfections or drifts (13) and noise, accentuated by bSSFP signal instability (24). However, they do not appear in the RSS T_2 map of Figure 5 thus demonstrating that four phase offsets provide sufficient robustness against these imperfections, in addition to the expected gain in T_2NR.

<Figure 5>

Average T_2 measured in centered and off-centre ROIs are displayed in online Supporting Figure S4. In both cases the T_2 values derived from both the bSSFP1and bSSFP2 protocols compare well with CPMG with a mean absolute difference of ~4.9-7.4% for bSSFP1 and ~3.6-6.4% for bSSFP2 across all the layers, and among the four T_2 maps.

In vivo Measurements

Sagittal τ_2 and T_2 maps for the two in vivo DESPOT2 protocols are displayed in Figure 6a and b, respectively, along with T_2 from SRC. The volunteer has a metallic dental retainer which induces a signal void and tight banding artifacts within the mouth. Observe how stretching the RF pulse in (b) also acts as a fat-suppression technique, making it impossible to measure the T_2 of adipose. Equivalent SNR efficiency to the bSSFP1 protocol was achieved by decreasing the sampling bandwidth (from 517 to 271 Hz/pix). In contrast to the uniform phantom, residual oscillations within the T_2 maps obtained with long TR/T_{RF} are well below the anatomical contrast and are thus negligible, except behind the metal retainer.

Sagittal T_1 and T_2 maps of the eight volunteers are shown in Figure 7. Hardware imperfections result in some errors in T_2, especially in the neck area, and close to dental braces or retainers (especially in volunteers v2, v7 and v8).

<**Figure 6**>

<Figure 7>

Figure 8 compares axial T_1 and T_2 maps from the three bSSFP, the two SPGR and the CPMG protocols listed in Table 1. The histograms of all five T_2 images are displayed for comparison, revealing how the three different DESPOT2 protocols yield comparable mean T_2 of ~50 ms in WM, the SE-based T_2 fit yields WM T_2 ~60 ms, while the mono-exponential fit from CPMG yields a significantly longer T_2 ~70 ms (corrected using StimFit). Crooijmans et al. also reported a mean WM T_2 of ~61 ms using a similar SE-based mono-exponential T_2 fit (14). The longer T_2 measured by CPMG, which is not observed in the agar phantom measurements (Supporting Figure S4 in the online supporting material), is consistent with in vivo literature values obtained using a comparable CPMG sequence and curve-fitting method (34).

<Figure 8>

The mean T_2 and standard deviation of various tissue types and brain organs were measured and averaged across the 8 volunteers for the SPGRb and bSSFP3 protocols. They are listed (with and without finite RF pulse correction) in Table 2 and compared to reported literature values, including previous DESPOT2 implementations at 1.5T (11), (35), (14) and 3T (17); and CPMG-based T_2 quantification accounting for stimulated echoes at 3T (34), and 4.7T (30). The values reported in bold (or superscript e) correspond to the DESPOT2-FM technique of Deoni at 3T, with $\alpha_1/\alpha_2/TR$ =15/65°/4.2 ms (17). Previous DESPOT2 implementations (11), (17), (35), did not include finite RF pulse corrections and thus they agree closely with our *uncorrected* T_2 measurements. Table 2 also includes the T_1 values because the accuracy of T_2 in DESPOT2 also depends on the T_1. As a consistency check we also provide the $T_2^* \leq T_2$ measured by ordinary least-squares mono-exponential fit on the multi-echo SPGR datasets as shown in Ref. (36).

<Table 2>

Discussion and Conclusions

In this study, we have derived general analytical solutions to remove band artefacts in DESPOT2 using any number of phase offsets greater than one, along with a mathematical analysis of the T_2 and T_2NR values. These expressions reduce processing time (using a standard PC) to merely a few seconds for a volume containing ~11.8 M voxels.

We have shown that using a greater number of phase offsets increases the T_2NR both in magnitude and in uniformity with respect to the off-resonance phase ϕ. For brevity, phantom T_2 maps derived from three phase offsets ($N=3$) were not presented, but accuracy and SNR results generally lie between the $N=2$ and $N=4$ case. The technique readily accommodates additional phase offsets and more than two flip angles to improve T_2 accuracy, uniformity, and/or SNR.

In the phantom, MT effects with low concentrations of agar (7g/L) attenuate the bSSFP signal only by ~0–4% and can thus be ignored. However, in vivo MT effects are significant and two approaches were tested to remove them: selecting flip angles ($\alpha=12°/58°$) to cancel the MTR of the bSSFP signals and stretching the RF pulse durations while using lower flip angles ($\alpha=9°/35°$). The preferred approach depends on the application, but if more than two flip angles are to be acquired (as in mc-DESPOT (27)), then stretching the RF pulse duration is the only option (provided the spatial-spectral effects of long T_{RF} are not a concern), since cancelling the MTR is possible only using two flip angles.

The three DESPOT2 protocols tested in this study yield a comparable mean WM T_2 of ~50 ms (T_2 histogram of Figure 8) in volunteer v2, despite significantly different bSSFP scan parameters (N, TR, α and T_{RF}). Conversely, the mean WM T_2 measured using single-echo spin echo at varying TE, fitted to a mono-exponential model, was longer (WM T_2 ~60 ms), and that using a 32-echo CPMG was even longer (WM T_2 ~70 ms). One reason for these discrepancies is that the CPMG and SE signals are complicated functions of T_1, T_2, α, slice profiles, B_0, MT, diffusion, TE and TR. A simple mono-exponential fit with CPMG is especially prone to overestimation of the true T_2 because of the presence of stimulated echoes (30) and more elaborate fitting procedures must be employed, such as Bloch equation simulations (37), EPG simulations (30), or using a generating function (34). A second explanation for these discrepancies lies in the existence of different water proton T_2 compartments ("pools"), known to exist especially in WM (38), (39). Assuming a single-component T_2 relaxation in the presence of three pools yields a different *apparent* T_2 depending on the sequence, i.e., each sequence applies a stronger weighting of a different component (such as the myelin water $T_{2,M}$), over the other two components (i.e., intra-cellular and extra-cellular T_2 pools of axonal water) (35). In fact, Crooijmans et al. (14) prefer to speak of a *spectrum* of T_2 values, and also observed that the in vivo WM single-component T_2 at 1.5 T from DESPOT2 is significantly lower (~45 ms) than that from single-echo spin echo (~61 ms). They attribute this difference to the complex tissue microstructure that results in a

broad spectrum of T_2 values, which different pulse sequences (i.e., bSSFP vs. spin echo) "see" with different weightings. In the case of simple chemical environments like agar gel, there is a single pool (or narrower spectrum) of water T_2, and thus both bSSFP and spin echo sequences measure the same T_2. This effect is also discussed by Stanisz et al. for CPMG data (33), where the T_2 from a mono-exponential fit corresponds to the arithmetic mean T_2 (~70 ms in WM) of a multi-exponential fit.

The measured T_2 values listed in Table 2 compare well with literature values, including those of Deoni et al. (11), (35), where finite RF pulse and MT effects were not corrected (WM T_2~54 ms), and those of Crooijmans et al. with corrections (WM T_2~45 ms) (14), (28). We note that the latter employ only one phase offset while higher-order shimming minimizes off-resonance effects; therefore the measured T_2 is likely lower due to some residual off-resonance bias (Figure 1b). The application of the finite RF pulse correction systematically lowers the T_2 by about ~7.5%, further biasing it from the reported CPMG T_2 values (WM T_2~53-55ms). Although this remaining discrepancy might be explained by residual MT bias, and/or sequence-dependent weighting (14), recent work (40) has shown that T_2 mapping based on EPG simulations of CPMG still overestimates T_2 in vivo by 3–5%, with respect to the full Shinnar Le Roux-based modelling.

Finally, proton density (M_0) maps corrected for banding artifacts can also be obtained analytically from DESPOT2 using even N (see online Supporting Figure S6, and Supporting Figure S7). Moreover, field inhomogeneity maps (ΔB_0), could be obtained by taking the inverse sine or cosine of Eq. (9)b, unwrapping the phase, and then substituting into Eq. (6). However, as explained in the additional online supporting material, M_0 is more easily and accurately obtained from the DESPOT1/VFA technique (41), (42), and robust techniques for mapping ΔB_0 already exist.

Appendix A

Derivation of Eq. (5)

The SSFP signal is defined as the magnitude of Eq. (1), which simplifies to

$$S_{SSFP}(\alpha,\phi,TR)=\frac{M_0\sqrt{E_2}(1-E_1)\sin\alpha\sqrt{1+2E_2\cos\phi+E_2^2}}{E_2(1-E_1)(1+\cos\alpha)\cos\phi+1-E_1\cos\alpha-E_2^2(E_1-\cos\alpha)}.$$

To calculate the slope *m*, assuming the on-resonance linearized equation (Eq. (3)), we must simplify

$$m(\phi,\alpha_1,\alpha_2,TR)=\frac{\frac{S_{SSFP}(\alpha_1,\phi,TR)}{\sin\alpha_1}-\frac{S_{SSFP}(\alpha_2,\phi,TR)}{\sin\alpha_2}}{\frac{S_{SSFP}(\alpha_1,\phi,TR)\cos\alpha_1}{\sin\alpha_1}-\frac{S_{SSFP}(\alpha_2,\phi,TR)\cos\alpha_2}{\sin\alpha_2}}.$$

Assuming $-\pi \le \phi \le \pi$, and $0 \le \alpha_{1,2} \le \pi/2$, the above simplifies to

$$m(\phi,TR)=\frac{E_1-E_2^2-E_2(1-E_1)\cos\phi}{1-E_1E_2^2+E_2(1-E_1)\cos\phi}.$$

Substituting *m* into Eq. (4), yields Eq. (5).

Appendix B

Derivation of Eq. (9)

Rearranging Eq. (5) to remove the logarithm, and accounting for a phase offset θ_n we have

$$\varepsilon_2^{\theta_n}=\frac{E_2+\cos(\phi+\theta_n)}{E_2^{-1}+\cos(\phi+\theta_n)}$$

which can be rearranged as $E_2^2+E_2(1-\varepsilon_2^{\theta_n})\cos(\phi+\theta_n)-\varepsilon_2^{\theta_n}=0$. Choosing θ_1=0, and θ_2=π, we obtain a system of two equations

$$\begin{aligned}E_2^2+E_2(1-\varepsilon_2^0)\cos\phi-\varepsilon_2^0=0\\ E_2^2-E_2(1-\varepsilon_2^\pi)\cos\phi-\varepsilon_2^\pi=0\end{aligned}.$$

Subtracting the equations we obtain

$-E_2\cos\phi(1-\varepsilon_2^0)-E_2\cos\phi(1-\varepsilon_2^\pi)=\varepsilon_2^0-\varepsilon_2^\pi \Rightarrow -E_2\cos\phi(2-\varepsilon_2^0-\varepsilon_2^\pi)=\varepsilon_2^0-\varepsilon_2^\pi$. Solving for $\cos\phi$ from the top equation and substituting results in

$$E_2^2=\frac{\varepsilon_2^0-2\varepsilon_2^0\varepsilon_2^\pi+\varepsilon_2^\pi}{2-\varepsilon_2^0-\varepsilon_2^\pi}.$$

Taking the logarithm on both sides and rearranging yields Eq. (9a), while Eq. (9b) is obtained by substituting for E_2 in the expression for $\cos\phi$. It can be shown in general that for any two phase offsets θ_1 and θ_2, such that $\theta_2-\theta_1=\pi$, the solution is

$$T_2 = -TR \Big/ \log\left(\sqrt{\frac{2\varepsilon_2^{\theta_1}\varepsilon_2^{\theta_2} - \varepsilon_2^{\theta_1} - \varepsilon_2^{\theta_2}}{\varepsilon_2^{\theta_1} + \varepsilon_2^{\theta_2} - 2}}\right)$$

$$\cos(\phi - \theta_1) = \frac{\varepsilon_2^{\theta_1} - \varepsilon_2^{\theta_2}}{\sqrt{(\varepsilon_2^{\theta_1} + \varepsilon_2^{\theta_2} - 2)(2\varepsilon_2^{\theta_1}\varepsilon_2^{\theta_2} - \varepsilon_2^{\theta_1} - \varepsilon_2^{\theta_2})}}.$$

While $\cos(\phi-\theta)$ is elegantly expressed above solely in terms of ε_2^{θ}, the following solution (obtained by simply rearranging Eq. (5)) is preferred to avoid phase-wrapping in regions of low SNR:

$$\cos(\phi - \theta_1) = \frac{\varepsilon_2^{\theta_1} - E_2^2}{E_2(1 - \varepsilon_2^{\theta_1})}.$$

Appendix C

Derivation of Eq. (16)

The partial derivative (with respect to T_1) in Eq. (15) is calculated from (Eq. (4))

$$T_2 = \tau_2(0) = \frac{-TR}{\log\left(\frac{m - E_1}{mE_1 - 1}\right)},$$

obtaining

$$\frac{\partial T_2}{\partial T_1} = \frac{E_1(m^2 - 1)\, TR^2}{(1 - mE_1)(m - E_1)\, T_1^2 \log\left(\frac{m - E_1}{mE_1 - 1}\right)^2}.$$

Substituting into the above

$$m = \frac{E_1 - E_2}{1 - E_1E_2},$$

and simplifying results in

$$\frac{\partial T_2}{\partial T_1} = \frac{E_1(1 - E_2^2)T_2^2}{E_2(1 - E_1^2)T_1^2}.$$

For the other two derivatives with respect to S, we apply the chain rule:

$$\frac{\partial T_2}{\partial S_i} = \frac{\partial T_2}{\partial m}\left(\frac{\partial m}{\partial y_1}\frac{\partial y_1}{\partial S_i} + \frac{\partial m}{\partial x_1}\frac{\partial x_1}{\partial S_i}\right).$$

The derivatives of the slope with respect to x or y are

$$m = \frac{y_2 - y_1}{x_2 - x_1},\ \frac{\partial m}{\partial y_1} = \frac{-1}{x_2 - x_1},\ \frac{\partial m}{\partial y_2} = \frac{1}{x_2 - x_1},\ \frac{\partial m}{\partial x_1} = \frac{y_2 - y_1}{(x_2 - x_1)^2},\ \frac{\partial m}{\partial x_2} = -\frac{y_2 - y_1}{(x_2 - x_1)^2}.$$

Moreover, using

$$y_i = \frac{S_i}{\sin\alpha_i}, \text{ and } x_i = \frac{S_i}{\tan\alpha_i},$$

we have $\frac{\partial y_i}{\partial S_i} = \frac{1}{\sin\alpha_i}$, and $\frac{\partial x_i}{\partial S_i} = \frac{1}{\tan\alpha_i}$.

Finally, $\partial T_2/\partial m$ is obtained similarly to $\partial T_2/\partial T_1$, resulting in

$$\frac{\partial T_2}{\partial m} = \frac{(1 - E_1^2)TR}{(1 - mE_1)(m - E_1)\log\left(\frac{m - E_1}{mE_1 - 1}\right)^2}.$$

Substituting all these results into Eq. (15) and simplifying, we obtain Eq. (16).

Acknowledgements

We gratefully acknowledge financial support from the Alberta Cancer Foundation, and the Alberta Cancer Research Institute. We also thank Philips Healthcare for technical support and Dr. Roger Luechinger for the PATI program used for data transfer.

References

1. Walker JM, Bulte JWM. Magnetic Resonance Neuroimaging: Methods and Protocols. Springer; 2011.

2. Ashburner J, Friston KJ. Voxel-based morphometry--the methods. Neuroimage 2000;11:805–21.

3. van Buchem MA, McGowan JC, Grossman RI. Magnetization transfer histogram methodology: its clinical and neuropsychological correlates. Neurology 1999;53:S23–S28.

4. Wang HZ, Riederer SJ, Lee JN. Optimizing the precision in T1 relaxation estimation using limited flip angles. Magn. Reson. Med. 1987;5:399–416.

5. Deoni SCL, Rutt BK, Peters TM. Rapid combined T1 and T2 mapping using gradient recalled acquisition in the steady state. Magn. Reson. Med. 2003;49:515–26.

6. Wang L, Schweitzer ME, Padua A, Regatte RR. Rapid 3D-T1 mapping of cartilage with variable flip angle and parallel imaging at 3.0T. J. Magn. Reson. Imaging 2008;27:154–61.

7. Manuel A, Li W, Jellus V, Hughes T, Prasad P V. Variable flip angle-based fast three-dimensional T1 mapping for delayed gadolinium-enhanced MRI of cartilage of the knee: need for B1 correction. Magn. Reson. Med. 2011;65:1377–83.

8. Yarnykh VL. Actual flip-angle imaging in the pulsed steady state: a method for rapid three-dimensional mapping of the transmitted radiofrequency field. Magn. Reson. Med. 2007;57:192–200.

9. Cheng H-LM, Wright GA. Rapid high-resolution T1 mapping by variable flip angles: accurate and precise measurements in the presence of radiofrequency field inhomogeneity. Magn. Reson. Med. 2006;55:566–74.

10. Deoni SCL. High-resolution T1 mapping of the brain at 3T with driven equilibrium single pulse observation of T1 with high-speed incorporation of RF field inhomogeneities (DESPOT1-HIFI). J. Magn. Reson. Imaging 2007;26:1106–11.

11. Deoni SCL, Peters TM, Rutt BK. High-resolution T1 and T2 mapping of the brain in a clinically acceptable time with DESPOT1 and DESPOT2. Magn. Reson. Med. 2005;53:237–41.

12. Deoni SCL, Ward HA, Peters TM, Rutt BK. Rapid T2 estimation with phase-cycled variable nutation steady-state free precession. Magn. Reson. Med. 2004;52:435–9.

13. Crooijmans HJA, Gloor M, Bieri O, Scheffler K. Influence of MT effects on T2 quantification with 3D balanced steady-state free precession imaging. Magn. Reson. Med. 2011;65:195–201.

14. Crooijmans HJA, Scheffler K, Bieri O. Finite RF pulse correction on DESPOT2. Magn. Reson. Med. 2011;65:858–62.

15. Aubert-Broche B, Grova C, Pike GB, Collins DL. Clustering of atlas-defined cortical regions based on relaxation times and proton density. Neuroimage 2009;47:523–32.

16. Liney GP, Knowles AJ, Manton DJ, Turnbull LW, Blackband SJ, Horsman A. Comparison of conventional single echo and multi-echo sequences with a fast spin-echo sequence for quantitative T2 mapping: application to the prostate. J. Magn. Reson. Imaging 1996;6:603–7.

17. Deoni SCL. Transverse relaxation time (T2) mapping in the brain with off-resonance correction using phase-cycled steady-state free precession imaging. J. Magn. Reson. Imaging 2009;30:411–7.

18. Wood TC, Wastling SJ, Barker GJ. Removing SSFP Banding Artifacts from DESPOT2 Images Using the Geometric Solution. In: Proc Intl Soc Magn Reson Med. Vol. 23. ; 2015. p. 1680.

19. Xiang QS, Hoff MN. Banding artifact removal for bSSFP imaging with an elliptical signal model. Magn. Reson. Med. 2014;71:927–933.

20. Zur Y, Stokar S, Bendel P. An analysis of fast imaging sequences with steady-state transverse magnetization refocusing. Magn. Reson. Med. 1988;6:175–93.

21. Zur Y, Wood ML, Neuringer LJ. Motion-insensitive, steady-state free precession imaging. Magn. Reson. Med. 1990;16:444–59.

22. Jung K-J. Synthesis methods of multiple phase-cycled SSFP images to reduce the band artifact and noise more reliably. Magn. Reson. Imaging 2010;28:103–18.

23. Lauzon ML, Frayne R. Analytical characterization of RF phase-cycled balanced steady-state free precession. Concepts Magn. Reson. Part A 2009;34A:133–143.

24. Dharmakumar R, Wright GA. Understanding steady-state free precession: A geometric perspective. Concepts Magn. Reson. Part A 2005;26:1–10.

25. Bieri O, Scheffler K. On the origin of apparent low tissue signals in balanced SSFP. Magn. Reson. Med. 2006;56:1067–74.

26. Bieri O, Scheffler K. SSFP signal with finite RF pulses. Magn. Reson. Med. 2009;62:1232–41.

27. Zhang J, Kolind SH, Laule C, Mackay AL. How Does Magnetization Transfer Influence mcDESPOT Results? Magn. Reson. Med. 2015;74:1327-1335.

28. Gloor M, Scheffler K, Bieri O. Quantitative magnetization transfer imaging using balanced SSFP. Magn. Reson. Med. 2008;60:691–700.

29. Lin F-H, Kwong KK, Belliveau JW, Wald LL. Parallel imaging reconstruction using automatic regularization. Magn. Reson. Med. 2004;51:559–67.

30. Lebel RM, Wilman AH. Transverse relaxometry with reduced echo train lengths via stimulated echo compensation. Magn. Reson. Med. 2010;64:1340–1346.

31. Oros-Peusquens AM, Laurila M, Shah NJ. Magnetic field dependence of the distribution of NMR relaxation times in the living human brain. MAGMA 2008;21:131–47.

32. Fedorov A, Beichel R, Kalpathy-Cramer J, et al. 3D Slicer as an image computing platform for the

Quantitative Imaging Network. Magn. Reson. Imaging 2012;30:1323–41.

33. Stanisz GJ, Odrobina EE, Pun J, Escaravage M, Graham SJ, Bronskill MJ, Henkelman RM. T1, T2 relaxation and magnetization transfer in tissue at 3T. Magn. Reson. Med. 2005;54:507–12.

34. Petrovic A, Scheurer E, Stollberger R. Closed-form solution for T2 mapping with nonideal refocusing of slice selective CPMG sequences. Magn. Reson. Med. 2015;73:818–827.

35. Deoni SCL, Williams SCR, Jezzard P, Suckling J, Murphy DGM, Jones DK. Standardized structural magnetic resonance imaging in multicentre studies using quantitative T1 and T2 imaging at 1.5 T. Neuroimage 2008;40:662–71.

36. Weiskopf N, Suckling J, Williams G, Correia MM, Inkster B, Tait R, Ooi C, Bullmore ET, Lutti A. Quantitative multi-parameter mapping of R1, PD*, MT, and R2* at 3T: A multi-center validation. Front. Neurosci. 2013;7:1–11.

37. Ben-Eliezer N, Sodickson DK, Block KT. Rapid and accurate T2 mapping from multi-spin-echo data using bloch-simulation-based reconstruction. Magn. Reson. Med. 2015;73:809–817.

38. MacKay A, Whittall K, Adler J, Li D, Paty D, Graeb D. In vivo visualization of myelin water in brain by magnetic resonance. Magn. Reson. Med. 1994;31:673–677.

39. Lenz C, Klarhöfer M, Scheffler K. Limitations of rapid myelin water quantification using 3D bSSFP. Magn. Reson. Mater. Physics, Biol. Med. 2010;23:139–151.

40. McPhee KC., Wilman AH. Comparison of Indirect and Stimulated Echo Compensated T2 Relaxometry Techniques : Extended Phase Graph vs Shinnar Le Roux Based Modelling. In: International Society of Magnetic Resonance in Medicine. Vol. 23. ; 2015. p. 1688.

41. Sabati M, Maudsley AA. Fast and high-resolution quantitative mapping of tissue water content with full brain coverage for clinically-driven studies. Magn. Reson. Imaging 2013;31:1752–9.

42. Volz S, Nöth U, Deichmann R. Correction of systematic errors in quantitative proton density mapping. Magn. Reson. Med. 2012;68:74–85.

43. Gold GE, Han E, Stainsby J, Wright G, Brittain J, Beaulieu C. Musculoskeletal MRI at 3.0 T : Relaxation Times and Image Contrast. Am. J. Neuroradiol. 2004;183:1479–1486.

Figure Captions

Figure 1: (a) Magnitude of the bSSFP signal as a function of α and ϕ for $T_1/T_2/TR$=1000/70/4.6 ms. (b) τ_2 normalized by the actual T_2, for $t=TR/T_2 \in [0, 1]$ and $\phi \in [-2\pi, 2\pi]$. (c) Plot of the approximate RSS T_2 normalized by the true T_2 using Eq. (9) within the range $t \in [0, 1]$ and $\phi \in [-2\pi, 2\pi]$ for N=3 and (d) for N=4.

Figure 2: Proposed DESPOT2 post-processing pipeline, with the choice of the exact or RSS solution. In addition to the bSSFP datasets, T_1 is required from DESPOT1 and the c_{RF}^{+} (normalized B_1 inhomogeneity field) from AFI.

Figure 3: (a) Analytical plots of the bSSFP signal (using Eq. (1)), for two different phase offsets (θ=0/π) and flip angles (α_1/α_2=11/57°), as a function of the off-resonance phase ϕ, and with or without the effect of finite RF pulse (T_{RF}=0/0.65 ms, using Eqs. (13)-(14)) for TR=4.6 ms in typical brain tissue (T_1/T_2=1000/70 ms). (b) Analytical τ_2^0, τ_2^π, and T_2 with or without finite RF pulse effects calculated from the bSSFP signals in (a) using Eqs. (5), and (9). (c) T_2NR plots (σ_1=10 ms, σ_s/M_0=0.002) calculated analytically using Eqs. (15-(18). (d) Corrected T_2 assuming T_{RF}=0.65 ms after making the following substitutions: $TR \rightarrow TR_{eff} = TR - 0.498\ T_{RF}$ (in Eq. (9) for the exact solution with N=2 or N=4), and $TR \rightarrow TR_{eff} = TR - 0.555\ T_{RF}$, (in Eq. (4) for the RSS solution with N=3 or N=4), showing the remaining oscillations.

Figure 4: (a) bSSFP0 image at α=11°, θ=π/2 and TR=9.2 ms. (b) Signal profile through the image in (a), displaying all four bSSFP signals. (c) Analytical T_2 map (with short T_{RF}) calculated using the four bSSFP datasets, the T_1 and the c_{RF} maps. (d) Profile through the T_2 map in (c), displaying both τ_2 signals, the final T_2 with TR/T_{RF2} =9.0/0.28 ms (solid black curve) and T_2 with TR/T_{RF2}=9.0/2.0 ms (dashed black curve).

Figure 5: a) Sagittal phantom images of the τ_2 and T_2 maps obtained from the bSSFP1 protocol, and b) the bSSFP2 protocol (Table 1). Results from Stochastic Region Contraction (DESPOT2-FM) technique are shown in the third row for both (a) and (b), and profiles through the 6th layer (red line) are shown to illustrate the differences. The colored intensity maps are percent difference between the exact-weighted and RSS solutions (N=4). The red arrow indicates an edge in T_2 arising from a combination of noise, mathematical singularity, and hardware imperfections, while the green arrows point to spatial-spectral effects.

Figure 6: a) In vivo (volunteer v2) τ_2 corresponding to four different phase offsets (θ=0, π, π/2, and 3π/2) and T_2 maps (calculated using the same techniques, including Stochastic Region

Contraction (DESPOT2-FM), as for the phantom in Figure 5) from bSSFP1 protocol (Table 1). b) Same maps in (a) obtained from the bSSFP2 data.

Figure 7: In vivo sagittal T_1 and T_2 maps (in ms) of the 8 volunteers scanned with protocols SPGRb and bSSFP3 (Table 1). Volunteers v2, v7, and v8 have signal voids in the mouth due to dental braces or metal retainers.

Figure 8: Axial T_1 maps from DESPOT1 (with SPGRa and SPGRb protocols), and T_2 from DESPOT2 (bSSFP1, bSSFP2 and bSSFP3 protocols in Table 1) compared to CPMG (single-component, mono-exponential fit), along with all 5 T_2 histograms for volunteer v2. Observe how the SE-based T_2 (WM T_2~60ms) lies between the DESPOT2 (WM T_2~50ms) and CPMG measurements (WM T_2~70ms). Spatial-spectral RF pulse effects in bSSFP2 cause underestimated T_2 in the scalp (arrow).

Supporting Figure S1: Measured bSSFP signal (blue) and predicted signal from Eq. 2 (orange), from an ROI in (a) the right occipital lobe, and in (b) the left putamen. (c) MTR curves as a function of flip angle and T_{RF} calculated as the percent difference between the two-pool and the single-pool signals. Two optimized flip angles (dashed vertical lines) can then be located to approximately cancel the MT effects in both WM and GM.

Supporting Figure S2: T2NR derived analytically and plotted in Mathematical (a) compared to a Monte Carlo T2NR simulation in MATLAB (b). Notice how assigning $\varepsilon_2^{\theta}=0$ wherever $E_1-m\leq 0$ (black curve in (b)) reduces the spike due to noise and mathematical singularity.

Supporting Figure S3: *Sin* ϕ and *cos* ϕ maps derived analytically using Eqs. (9)- ((10) from a) the bSSFP1 protocol, and b) from the bSSFP2 protocol. Arrows indicate discontinuities (slight mismatches in band locations across the different bSSFP datasets) due to noise and hardware imperfections that are magnified by signal instabilities (24).

Supporting Figure S4: Measured T_2 (in both central (solid bar) and off-centre (hatched) ROIs) in each layer of the phantom for the DESPOT2 protocol with short TR/T_{RF} (bSSFP1) and (b) long TR/T_{RF} (bSSFP2). For comparison the T_2 measured using the 32-echo CPMG is also displayed in green.

Supporting Figure S5: Simulated relative M_0 and *cos* ϕ derived using bSSFP scan parameters $\theta_1/\theta_2/\alpha_1/\alpha_2/TR$= 0/$\pi$/11/57°/4.6 ms, and physical parameters $M_0/T_1/T_2$=1.00/1000/70 ms with same Gaussian noise variances σ_1=10, σ_S=0.002 defined in Eq. (13) and used in Figure 2.

Supporting Figure S6: (a) Phantom M_0 maps (in arbitrary units) derived from the bSSFP1 protocol with short TR/T_{RF2}=4.8/0.55 ms. (b) M_0 maps obtained from the bSSFP2 protocol with long TR/T_{RF2}=9.0/2.0 ms. SRC results are displayed in the third row, along with a difference map between SRC and the exact solution with N=4.The M_0 calculated from the DESPOT1 (a.k.a. VFA) technique is also shown for comparison. Note that B_1^- correction was applied by assuming RF symmetry: $c_{RF}^+ = c_{RF}^-$.

Supporting Figure S7: (a) M_0 maps (in % H_20) of volunteer v2 derived from the bSSFP1 protocol, (b) the bSSFP2 protocol, and (c) the SPGRa protocol (via DESPOT1/VFA technique). Note that c_{RF}^- correction was performed using the N4ITK bias-field correction algorithm in 3D Slicer.

Tables

Pulse Sequence	Voxel Resolution (mm)	TR_1/TR_2 /TE/N_{echo} (ms)	α_1/α_2 (°)	T_{RF1}/T_{RF2} (ms)	BW (Hz/ pix)	SENSE Factors (AP×RL)	Δf_0 (Hz)
AFI	3.5×5.0×5.0	25/125/2.8/1	60/–	0.294/—	221	1.0×1.0	—
SPGRa	1.0×1.0×1.3	21/—/2.3n/8	5/25	0.026/0.12	517	1.4×1.2	—
SPGRb	1.0×1.0×1.5	24/—/2.3n/9	5/25	0.026/0.12	517	1.2×1.2	—
bSSFP0	1.2×1.2×1.2	9.2/—/4.6/1	11/57	0.058/0.28	517	1.0×1.0	27.17, 81.52
bSSFP1	1.1×1.1×1.1	4.8/—/2.4/1	12/58	0.064/0.55	517	1.2×1.0	0, 52.08, 104.17, 156.25
bSSFP2	1.1×1.1×1.1	9.0/—/4.5/1	9/35	0.59/2.0	271	1.5×1.5	0, 27.78, 55.56, 83.33
bSSFP3	1.0×1.0×1.2	4.4/—/2.2/1	11/57	0.058/0.60	517	1.0×1.0	0, 75.76, 151.52
CPMG*	1.2×1.2×5.0	2000/—/15n/32	90/—	—/—	217	1.0×1.0	—

Table 1: MRI scan parameters used both on the phantom and in vivo. Except for the 2D CPMG scan, the field-of-view was 240×240×170 cm^3, and hard, non-selective RF pulses were used in all cases. *Note that for CPMG in vivo the echo spacing was 10 ms.

Organ / Tissue	Corr. T_2 (ms)	Uncorr. T_2 (ms)	Literature T_2 (ms)		T_2^* (ms)	T_1 (ms)
			1.5 T	3 T, 4.7T[g]		
Putamen	62.7 (2.4)	67.6 (2.5)	71(7)[b]	**69(3)[e]**, 57(3)[f], 55(3)[g]	45.2 (4.4)	1442 (85)
Caudate	72.9 (3.2)	78.4 (4.0)	89(6)[a], 75(8)[b], 59[c], 59(3)[d]	**82(3)[e]**, 63(5)[f], 60(3)[g]	49.0 (3.9)	1563 (83)
Splenium	54.7 (3.8)	58.8 (4.2)	43(1)[d]	64(4)[g]	40.2 (1.9)	1027 (63)
Genu	48.8 (2.4)	52.4 (2.7)			38.3 (2.9)	956 (43)
Globus Pallidus	50.4 (3.3)	54.2 (3.6)		45(1)[f], 38(2)[g]	29.8 (2.8)	1212 (47)
Frontal WM R	47.7 (2.4)	51.2 (2.6)	53(4)[b], 40(2)[d]	**50(2)[e]**, 53(8)[f], 53(3)[g]	41.8 (2.9)	986 (42)
Frontal WM L	47.6 (2.1)	51.1 (2.3)	53(4)[b], 40(2)[d]	**50(2)[e]**, 53(8)[f], 53(3)[g]	41.7 (2.9)	983 (33)
Occipital WM R	53.8 (2.7)	57.8 (3.0)		55(1)[g]	45.1 (2.2)	1020 (35)
Occipital WM L	51.8 (1.6)	55.7 (1.8)		55(1)[g]	44.0 (1.6)	1024 (36)
WM (mean)	50.6 (1.3)	54.4 (1.4)	54(4)[a], 45[c]		45.7 (1.5)	1057 (34)
GM (mean)	67.0 (2.1)	71.8 (2.0)	71(28)[d]		56.3 (2.5)	1544 (81)
Muscle (mean)	36.5 (2.3)	39.3 (2.5)	35(4)[h]	32(2)[h]	22.8 (0.8)	1327 (49)
Adipose (mean)	99.1 (4.6)	106 (5)	165(6)[h]	133(5)[h]	NA	427 (20)

Table 2: Corrected and uncorrected T_2 (and standard deviations) in various brain regions across the 8 volunteers. The mean tissue values were measured from segmented T_2 histograms, while the regional values were measured in ROIs identified manually. References are: a:(11), b:(35), c:(14), d:(28), e:(17), f:(34), g:(30), h:(43). Values in bold are from DESPOT2-FM (see text). Note that the T_2^* of adipose cannot be measured by simple mono-exponential fit due to J-coupling.

a

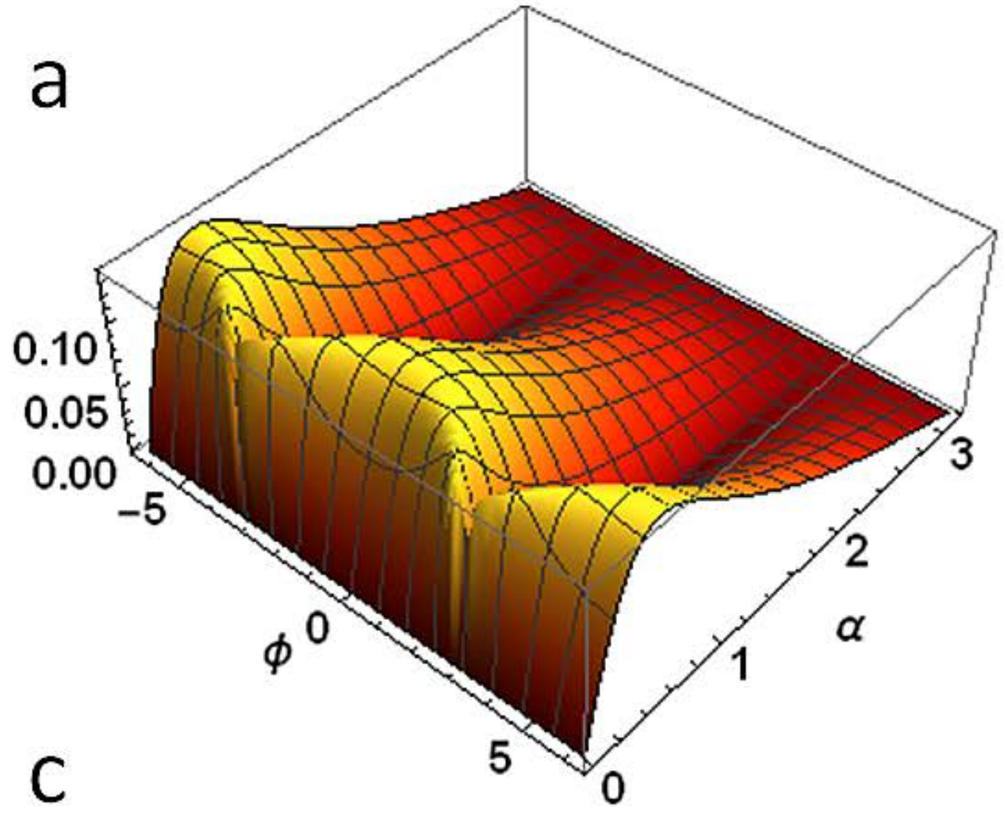
0.10
0.05
0.00
−5
ϕ
0
5
1
2
3
α

b

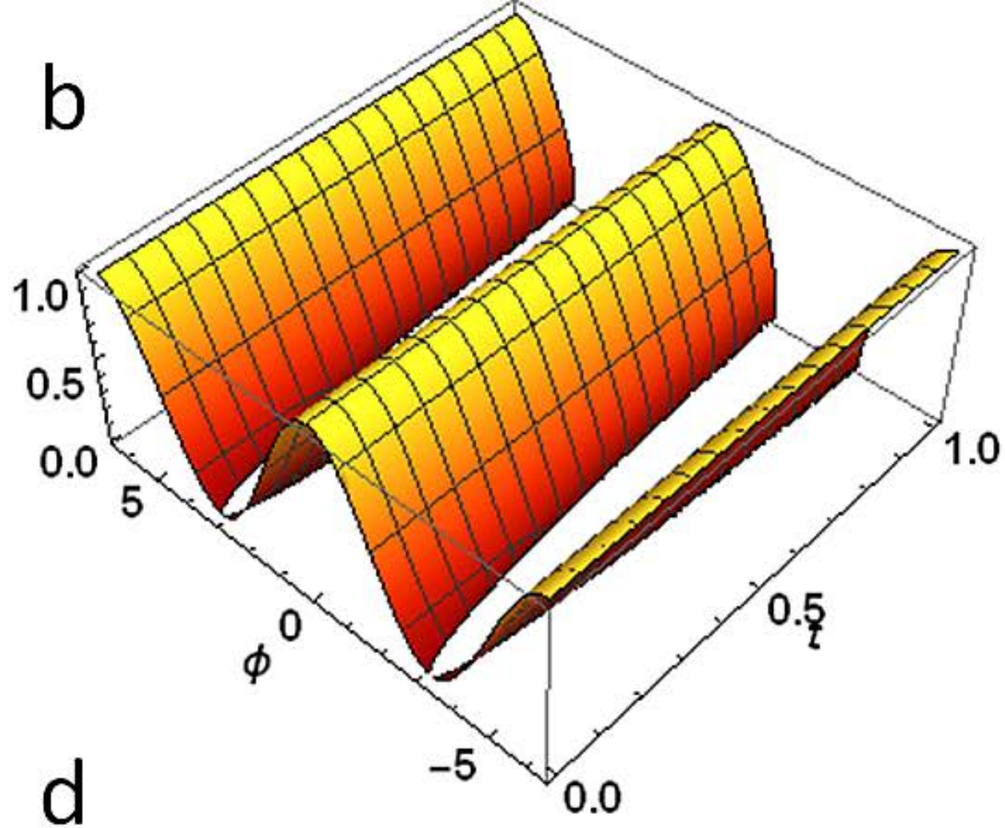
1.0
0.5
0.0
5
ϕ
0
−5
0.5
1.0
t
0.0

c

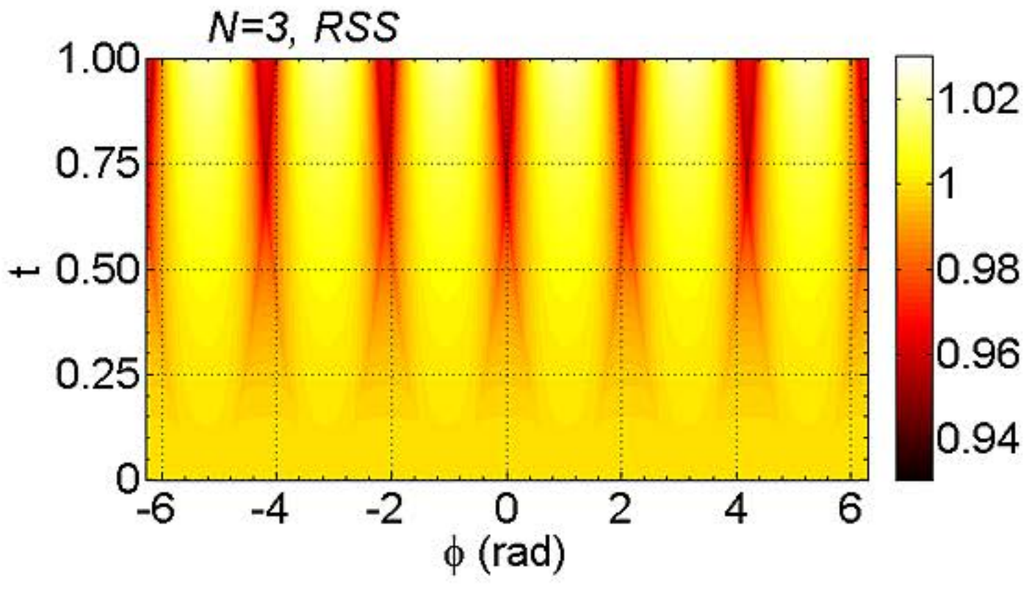
N=3, RSS
1.00
0.75
0.50
0.25
0
t
-6
-4
-2
0
2
4
6
ϕ (rad)
1.02
1
0.98
0.96
0.94

d

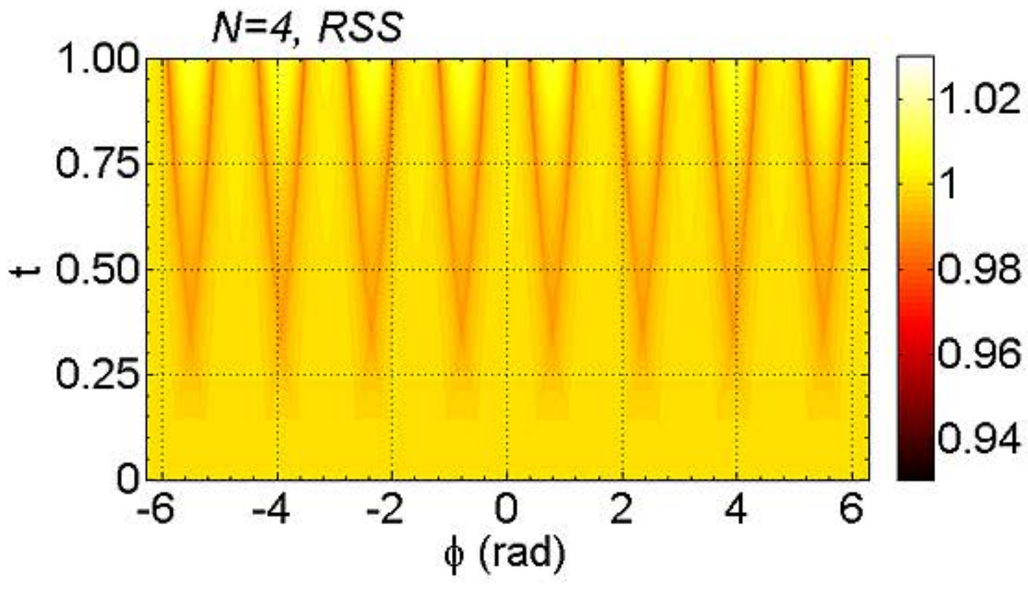
N=4, RSS
1.00
0.75
0.50
0.25
0
t
-6
-4
-2
0
2
4
6
ϕ (rad)
1.02
1
0.98
0.96
0.94

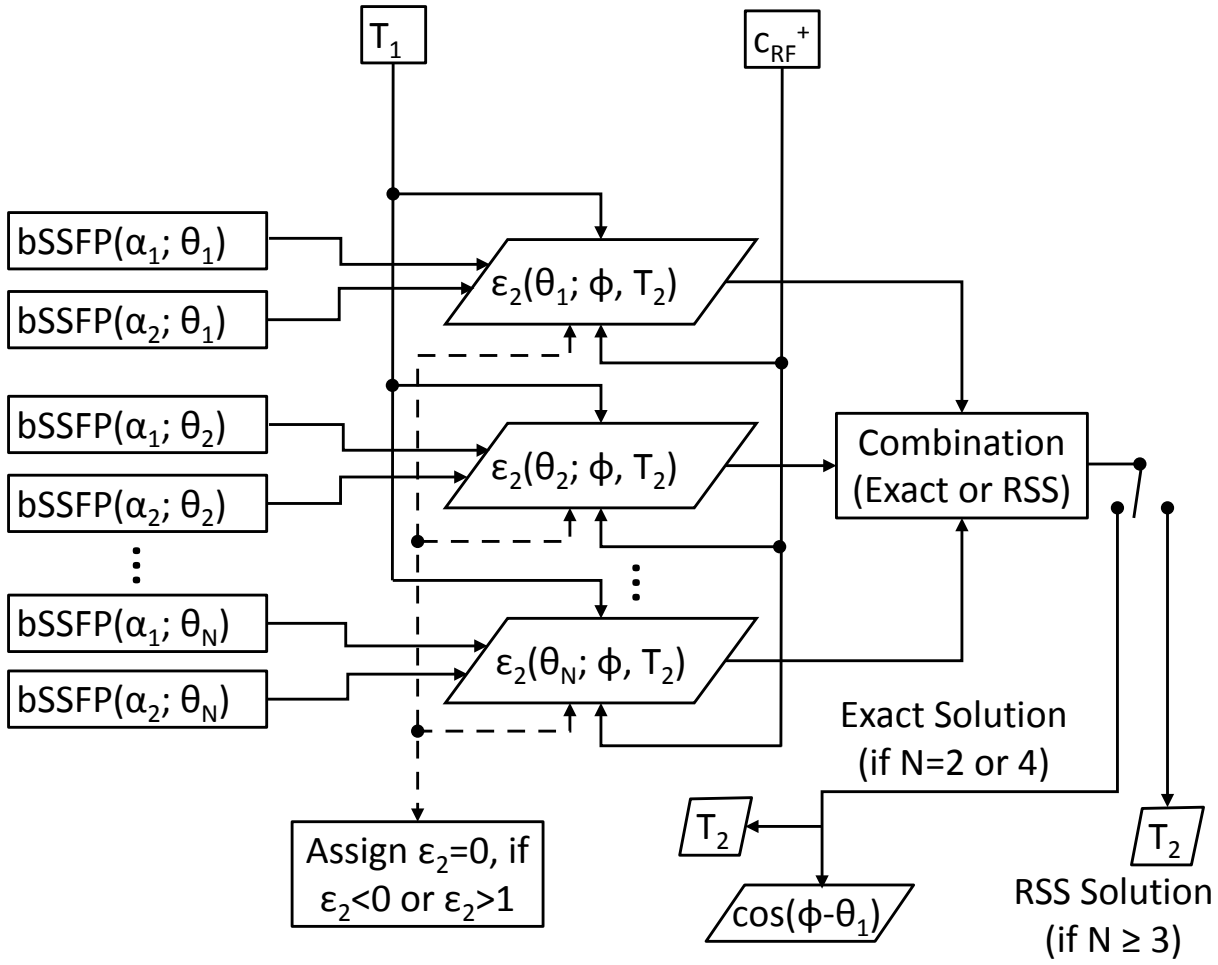
T_1
c_{RF}^+
bSSFP(α_1; θ_1)
bSSFP(α_2; θ_1)
$\varepsilon_2(\theta_1; \phi, T_2)$
bSSFP(α_1; θ_2)
bSSFP(α_2; θ_2)
$\varepsilon_2(\theta_2; \phi, T_2)$
Combination
(Exact or RSS)
bSSFP(α_1; θ_N)
bSSFP(α_2; θ_N)
$\varepsilon_2(\theta_N; \phi, T_2)$
Exact Solution
(if N=2 or 4)
T_2
T_2
RSS Solution
(if N ≥ 3)
Assign ε_2=0, if
ε_2<0 or ε_2>1
cos(ϕ-θ_1)

a

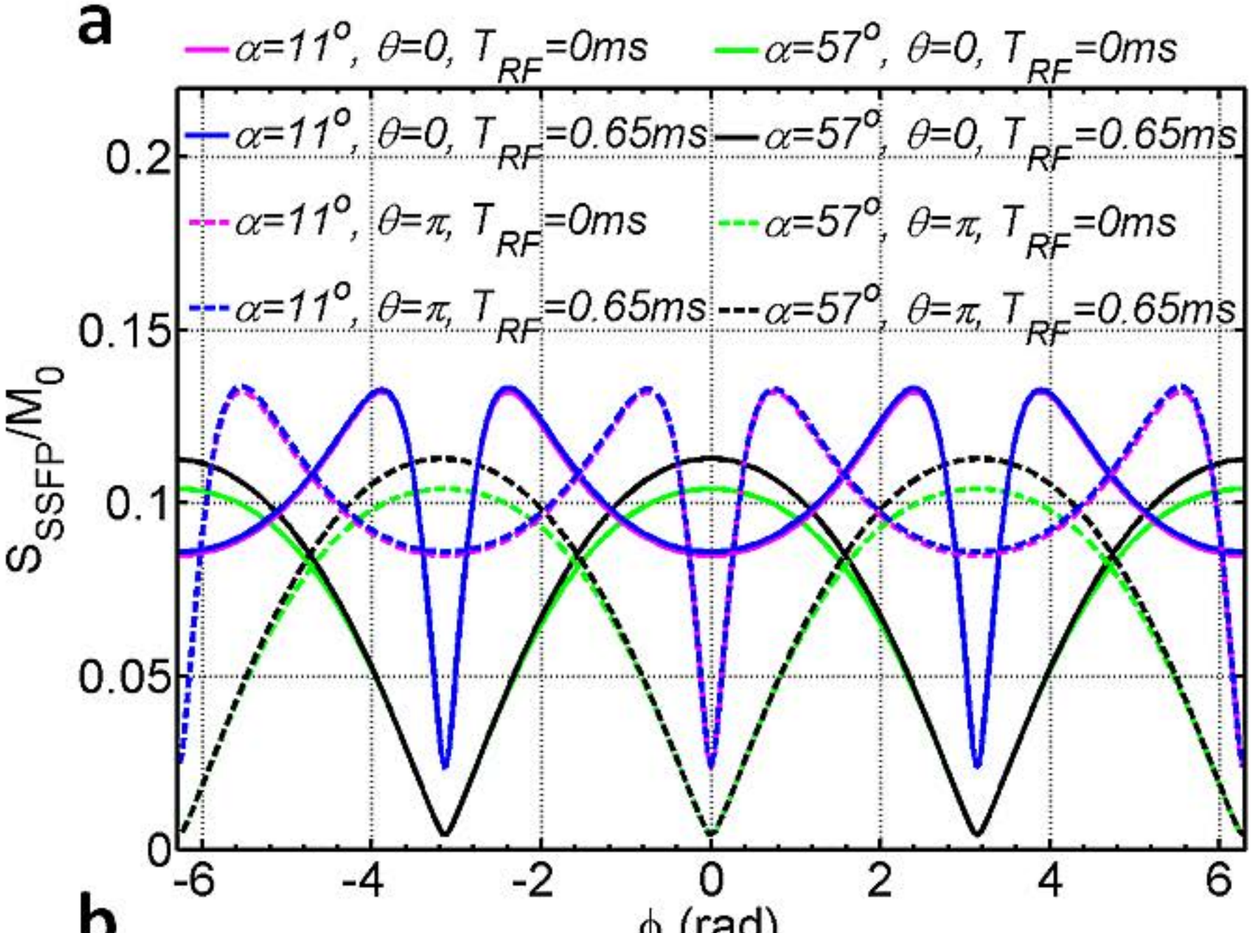
α=11°, θ=0, T_RF=0ms
α=57°, θ=0, T_RF=0ms
α=11°, θ=0, T_RF=0.65ms
α=57°, θ=0, T_RF=0.65ms
α=11°, θ=π, T_RF=0ms
α=57°, θ=π, T_RF=0ms
α=11°, θ=π, T_RF=0.65ms
α=57°, θ=π, T_RF=0.65ms
S_SSFP/M_0
0.2
0.15
0.1
0.05
0
-6
-4
-2
0
2
4
6
ϕ (rad)

b

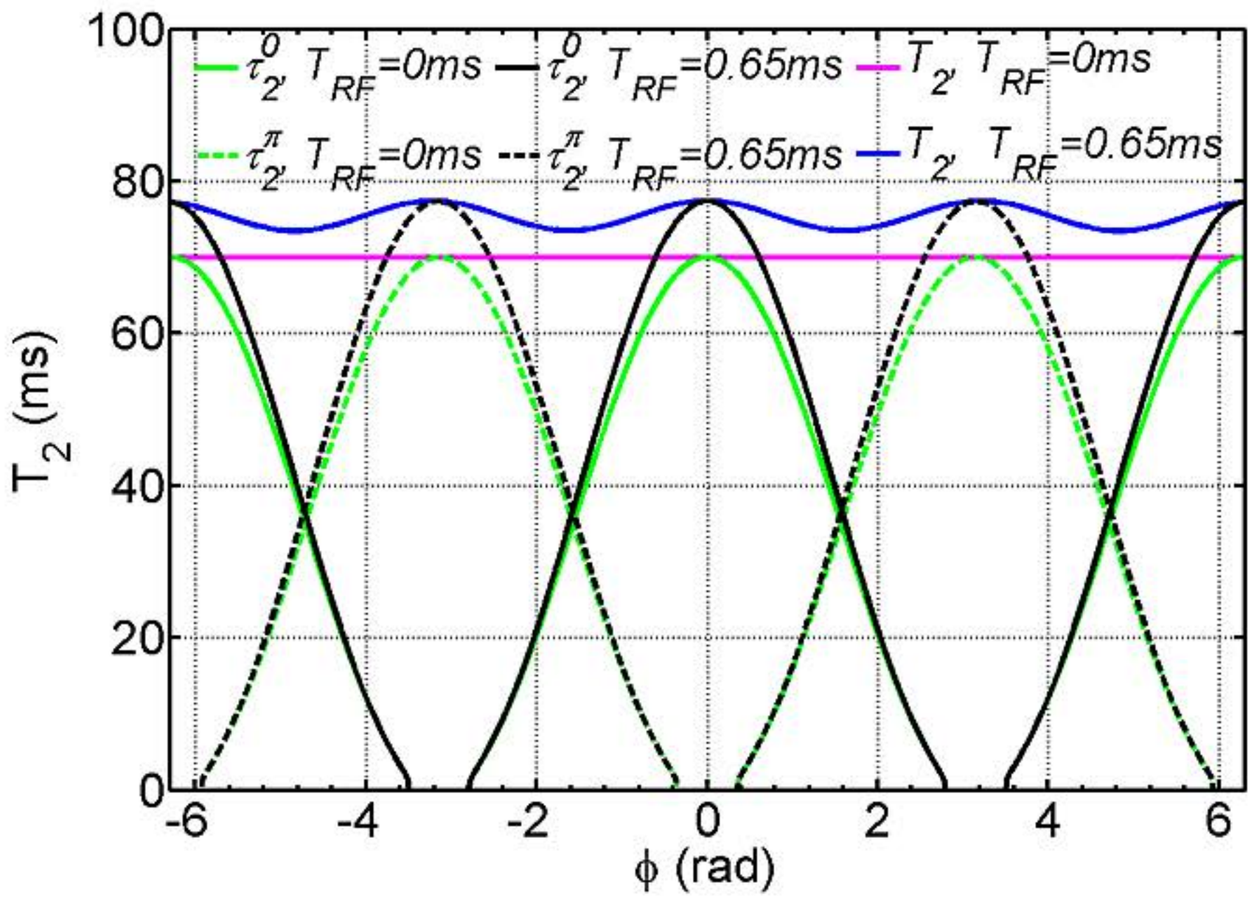
τ'_2 T_RF=0ms
τ'_2 T_RF=0.65ms
T_2' T_RF=0ms
τ^π_2' T_RF=0ms
τ^π_2' T_RF=0.65ms
T_2' T_RF=0.65ms
T_2 (ms)
100
80
60
40
20
0
-6
-4
-2
0
2
4
6
ϕ (rad)

c

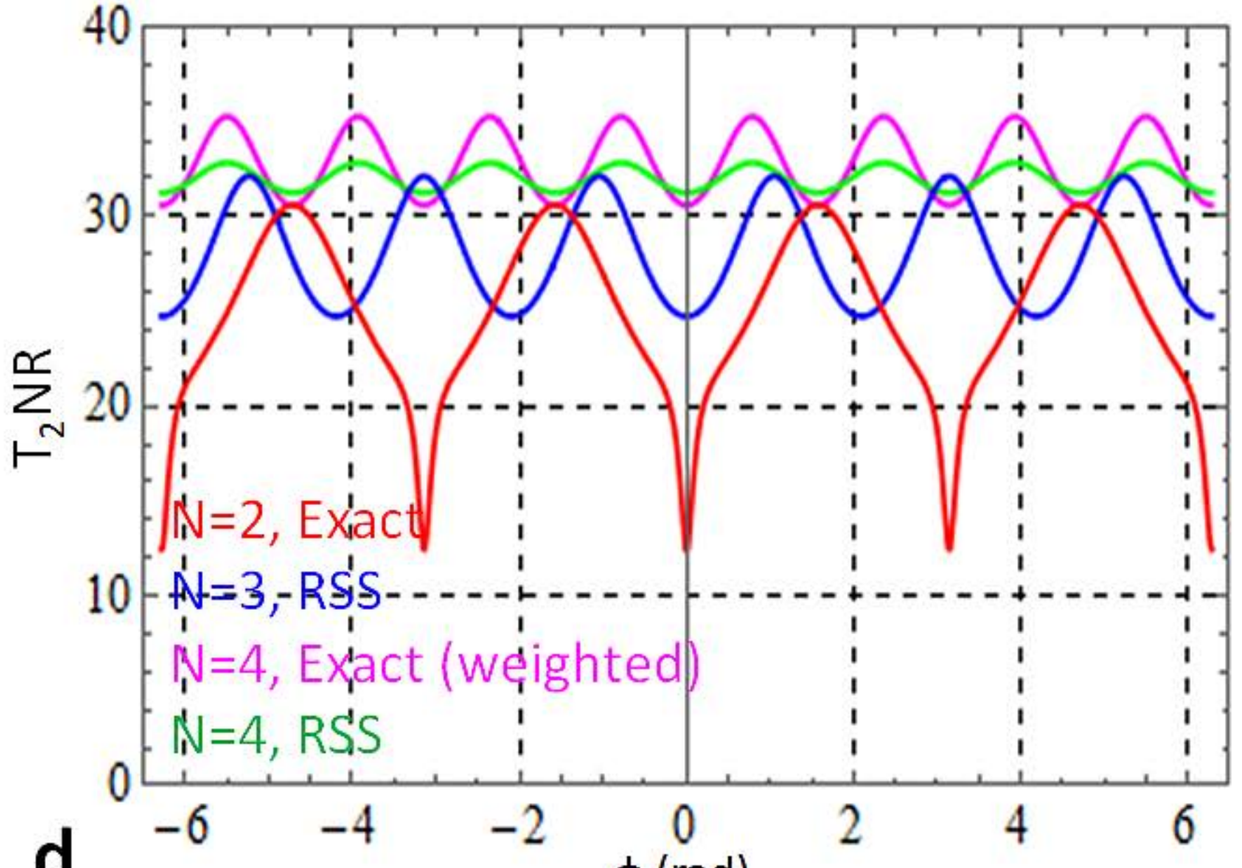
T_2NR
40
30
20
10
0
N=2, Exact
N=3, RSS
N=4, Exact (weighted)
N=4, RSS
-6
-4
-2
0
2
4
6
ϕ (rad)

d

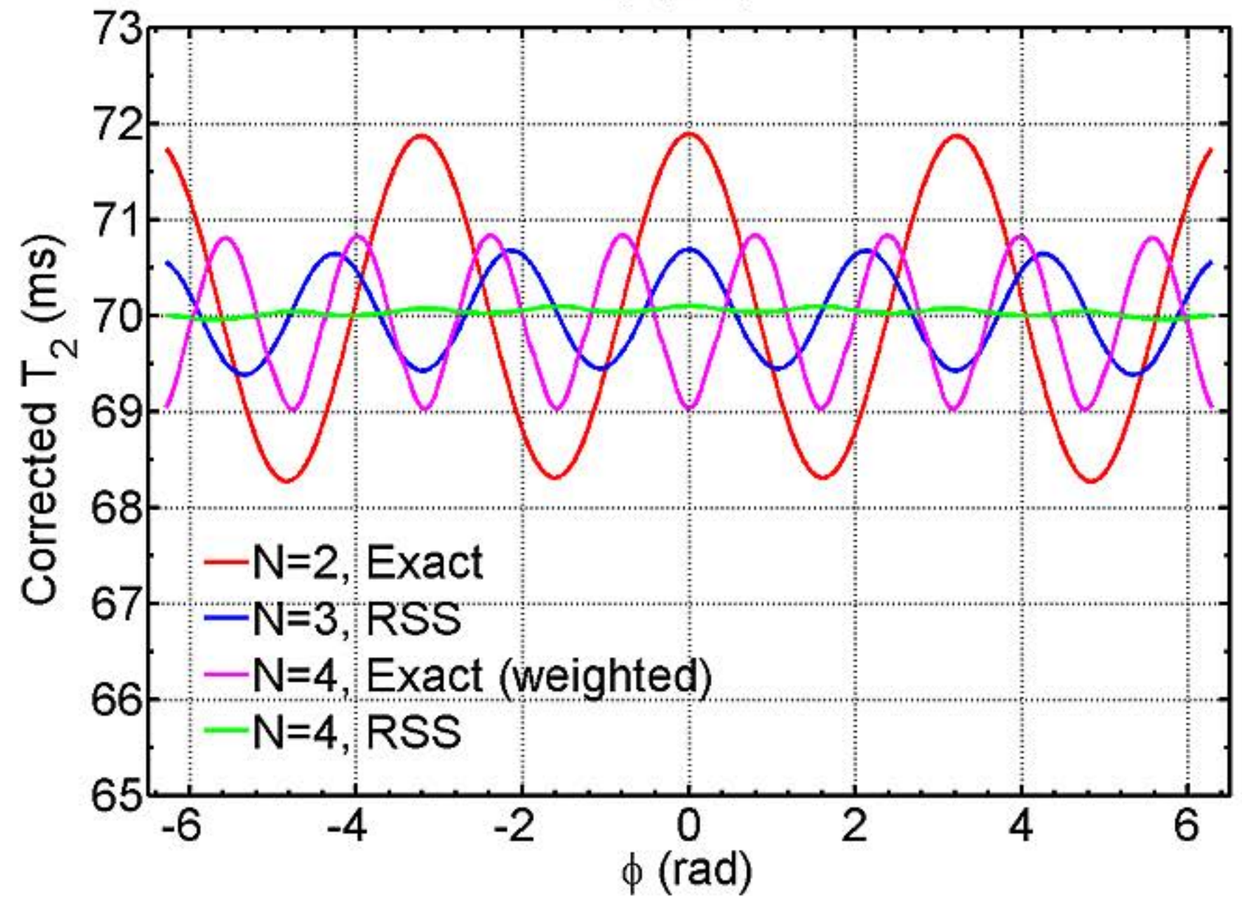
Corrected T_2 (ms)
73
72
71
70
69
68
67
66
65
N=2, Exact
N=3, RSS
N=4, Exact (weighted)
N=4, RSS
-6
-4
-2
0
2
4
6
ϕ (rad)

a

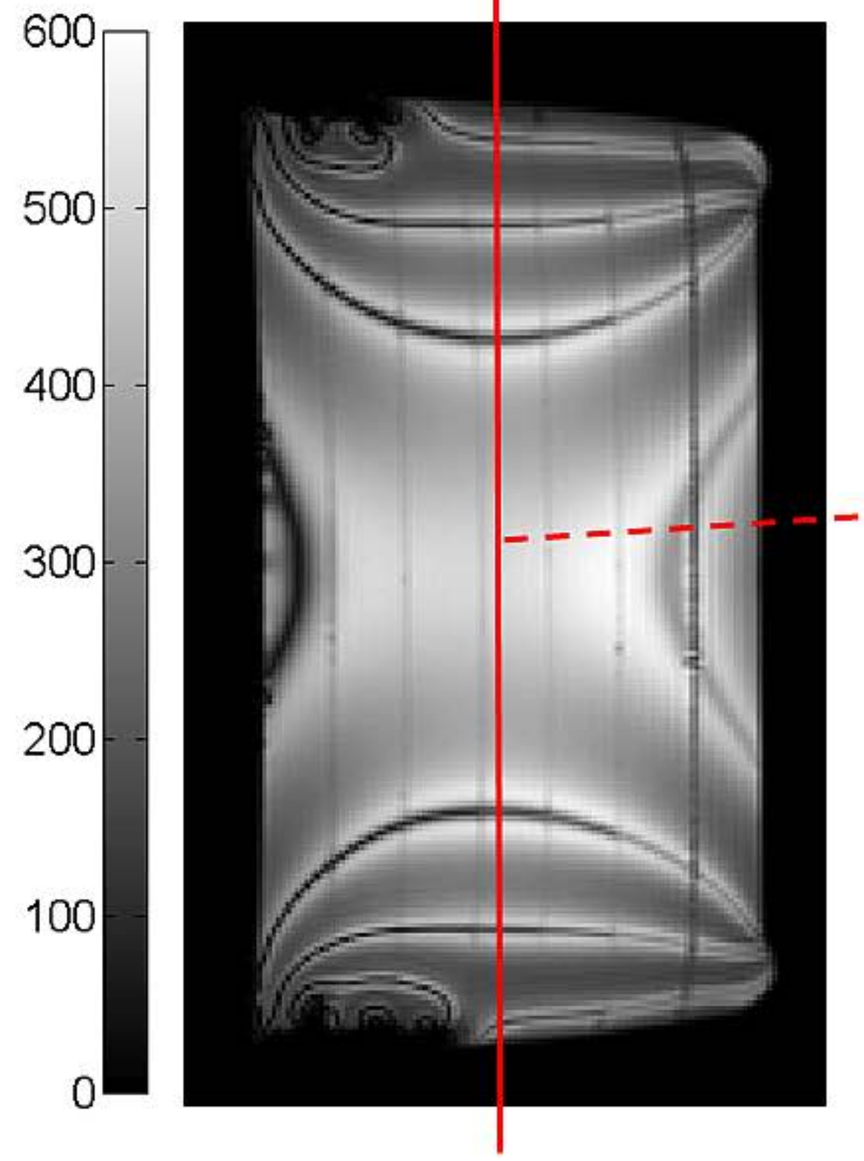
600
500
400
300
200
100
0

b

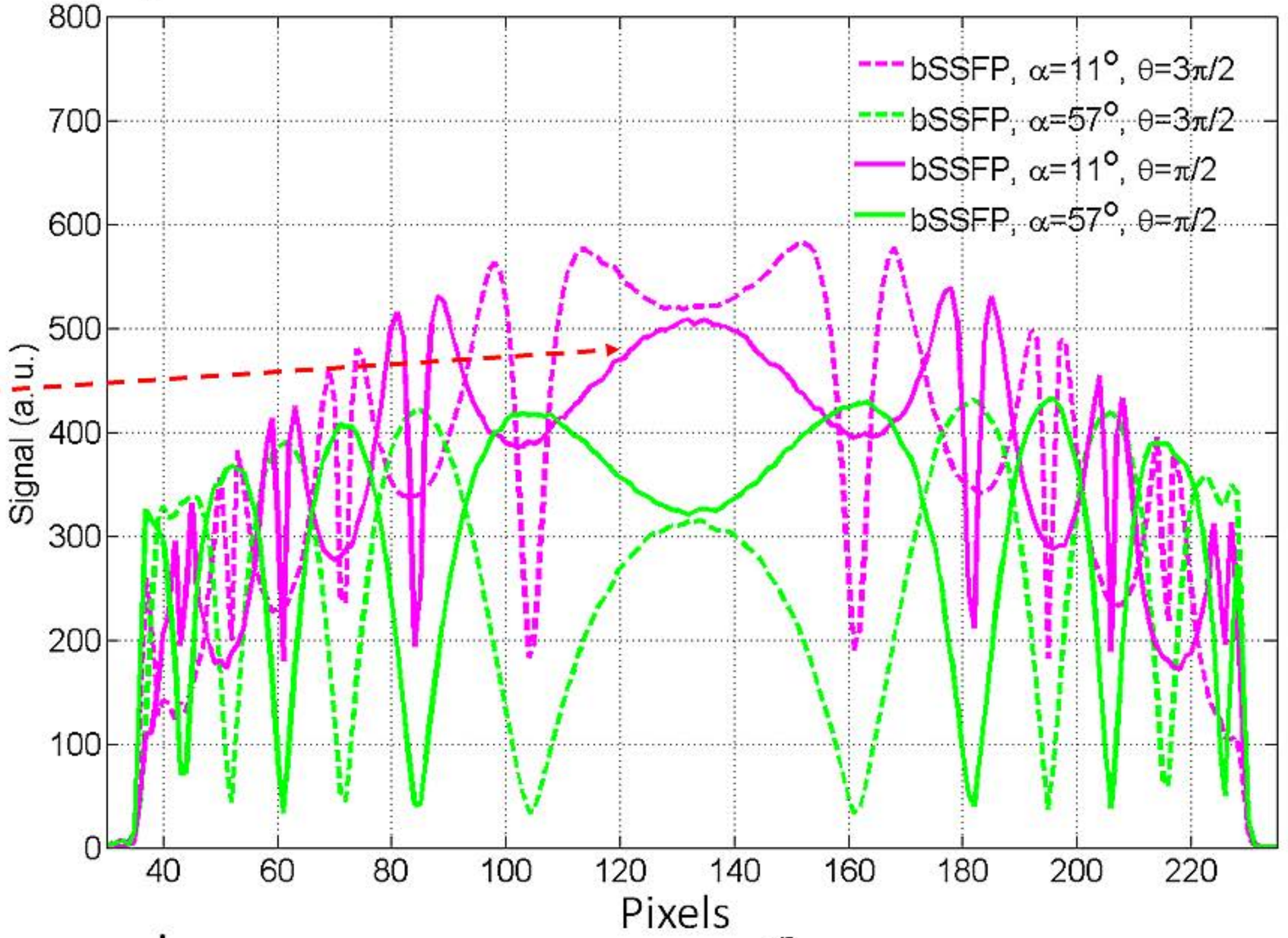
bSSFP, α=11°, θ=3π/2
bSSFP, α=57°, θ=3π/2
bSSFP, α=11°, θ=π/2
bSSFP, α=57°, θ=π/2
Signal (a.u.)
800
700
600
500
400
300
200
100
0
40
60
80
100
120
140
160
180
200
220
Pixels

c

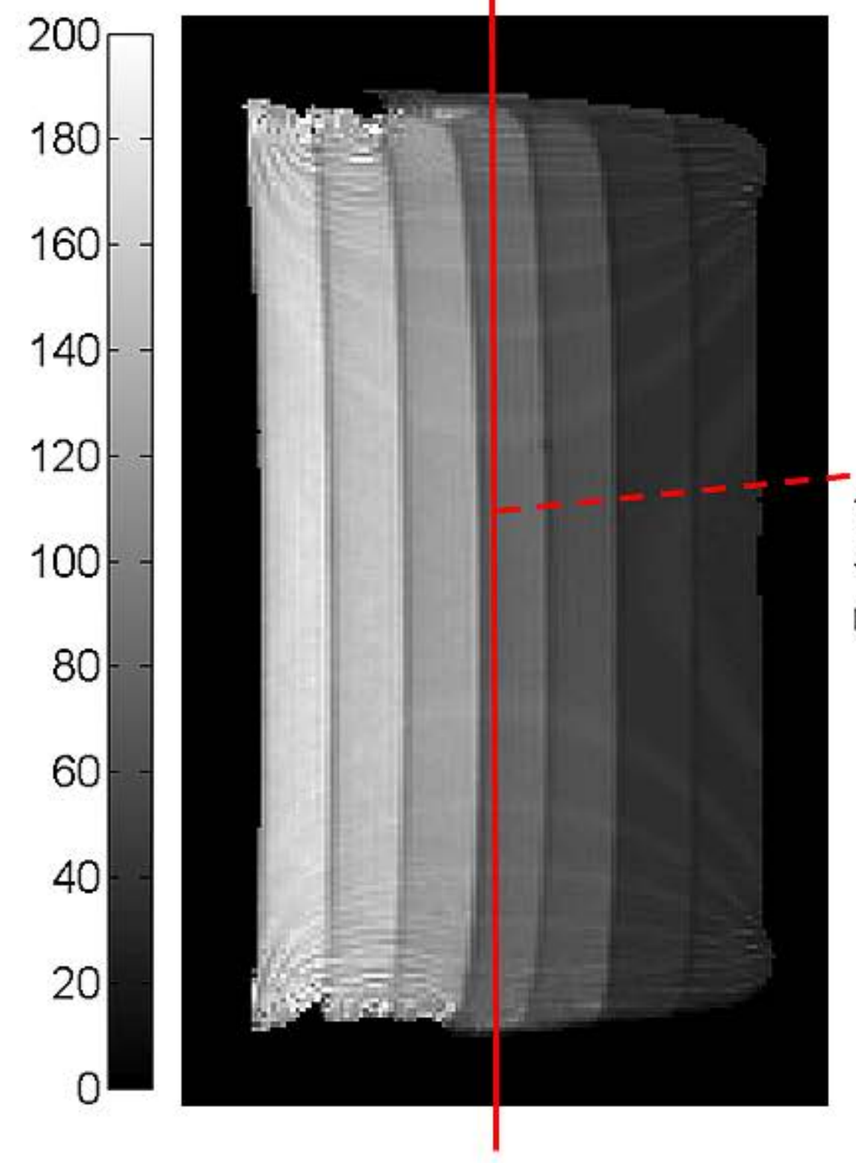
200
180
160
140
120
100
80
60
40
20
0

d

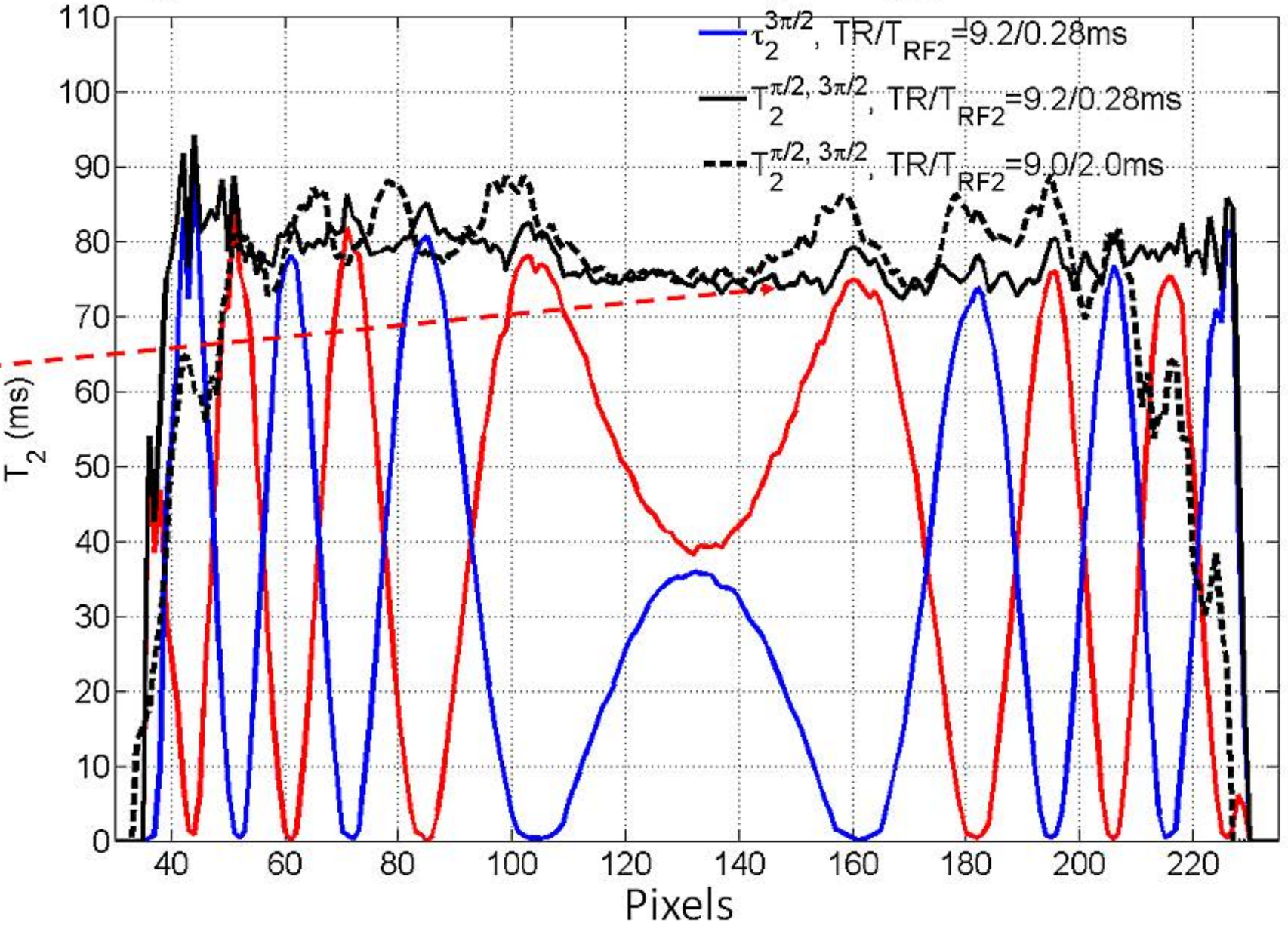
τ2π/2, TR/TRF2=9.2/0.28ms
τ23π/2, TR/TRF2=9.2/0.28ms
T2π/2, 3π/2, TR/TRF2=9.2/0.28ms
T2π/2, 3π/2, TR/TRF2=9.0/2.0ms
T2 (ms)
110
100
90
80
70
60
50
40
30
20
10
0
40
60
80
100
120
140
160
180
200
220
Pixels

a

τ_2, θ=0 | τ_2, θ=π | τ_2, θ=π/2 | τ_2, θ=3π/2

T_2, θ= 0, π | T_2, θ=π/2, 3π/2 | T_2, N=4, Exact | T_2, N=4, RSS

T_2, θ= 0, π, SRC | T_2, θ= π/2, 3π/2, SRC | T_2, N=4, SRC | % diff, RSS-Exact

(ms) 200 150 100 50 0

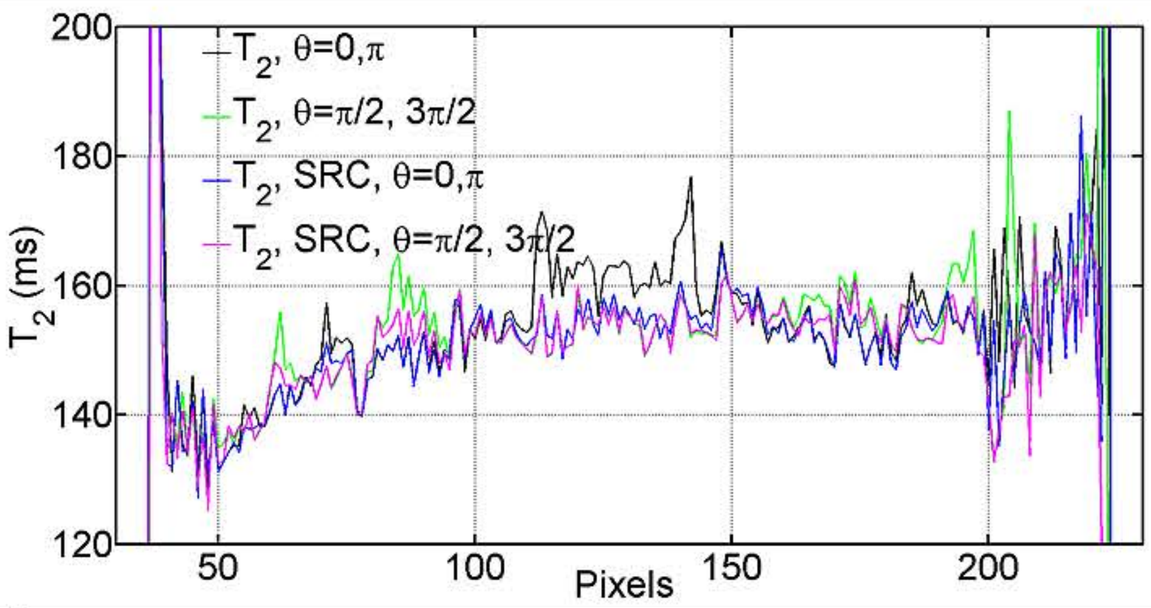

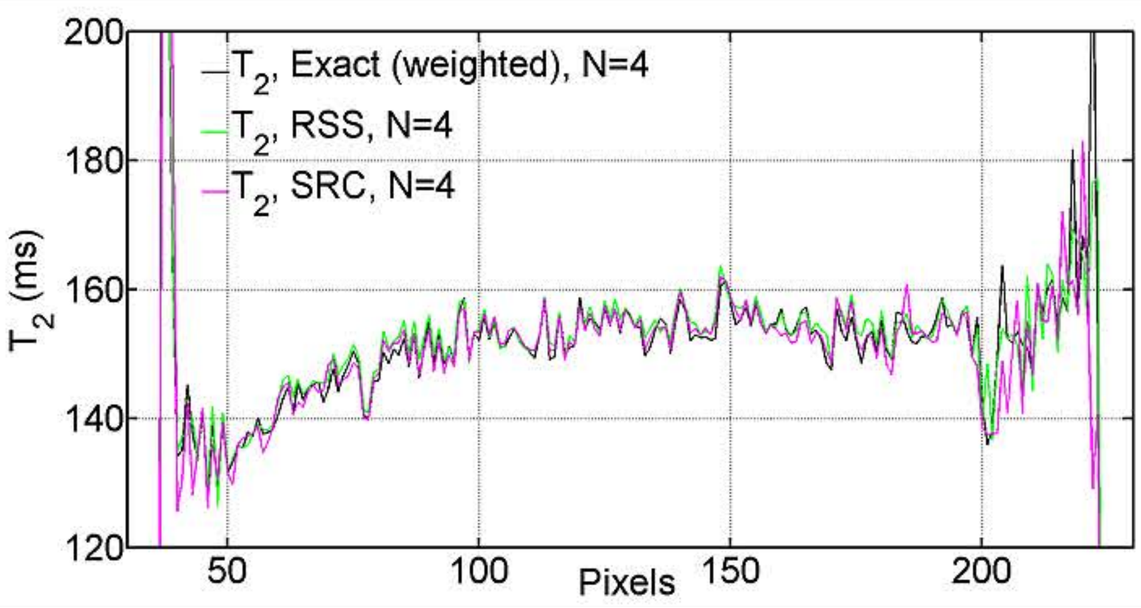

b

τ_2, θ=0 | τ_2, θ=π | τ_2, θ=π/2 | τ_2, θ=3π/2

T_2, θ= 0, π | T_2, θ=π/2, 3π/2 | T_2, N=4, Exact | T_2, N=4, RSS

T_2, θ= 0, π, SRC | T_2, θ= π/2, 3π/2, SRC | T_2, N=4, SRC | % diff, RSS-Exact

(%) 20 10 0 -10 -20

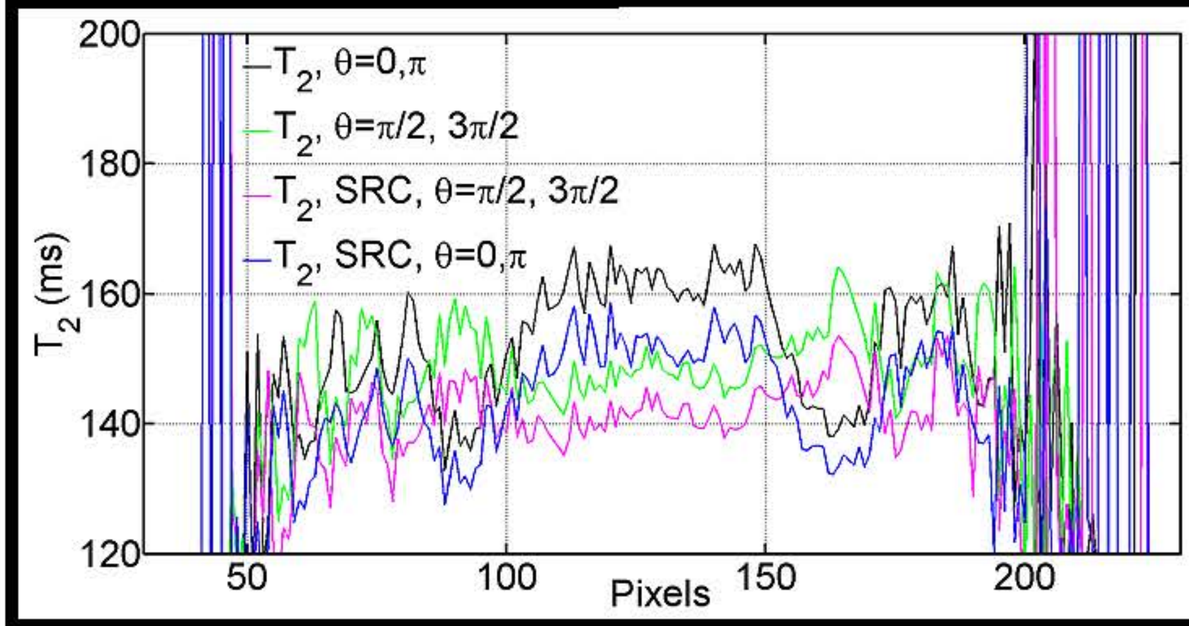

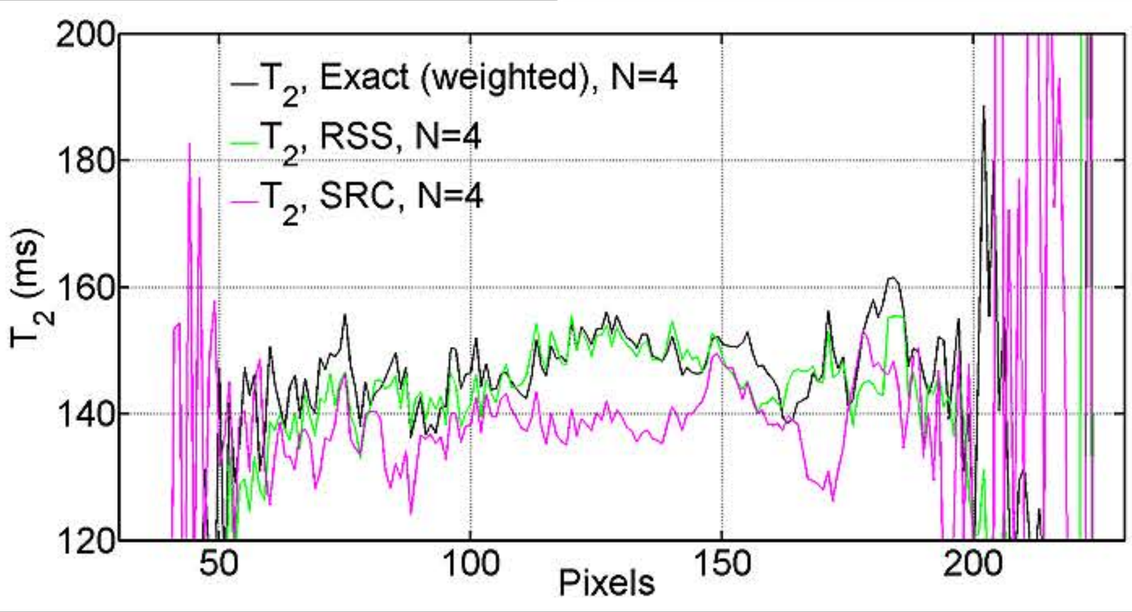

a τ_2^{0} τ_2^{π} $\tau_2^{\pi/2}$ $\tau_2^{3\pi/2}$

$T_2^{0,\pi}$ $T_2^{\pi/2,3\pi/2}$ T_2 Exact T_2 RSS

$T_2^{0,\pi}$ SRC $T_2^{\pi/2,3\pi/2}$ SRC T_2, N=4 SRC % diff, N=4, RSS-Exact

b τ_2^{0} τ_2^{π} $\tau_2^{\pi/2}$ $\tau_2^{3\pi/2}$

$T_2^{0,\pi}$ $T_2^{\pi/2,3\pi/2}$ T_2 Exact T_2 RSS

$T_2^{0,\pi}$ SRC $T_2^{\pi/2,3\pi/2}$ SRC T_2, N=4 SRC % diff, N=4, RSS-Exact

0 50 100 150 200 (ms)

-20 -10 0 10 20 (%)

3000
2500
2000
1500
1000
500
0
T1
v1
v2
v3
v4
T2
200
180
160
140
120
100
80
60
40
20
0
3000
2500
2000
1500
1000
500
0
T1
v5
v6
v7
v8
T2
200
180
160
140
120
100
80
60
40
20
0

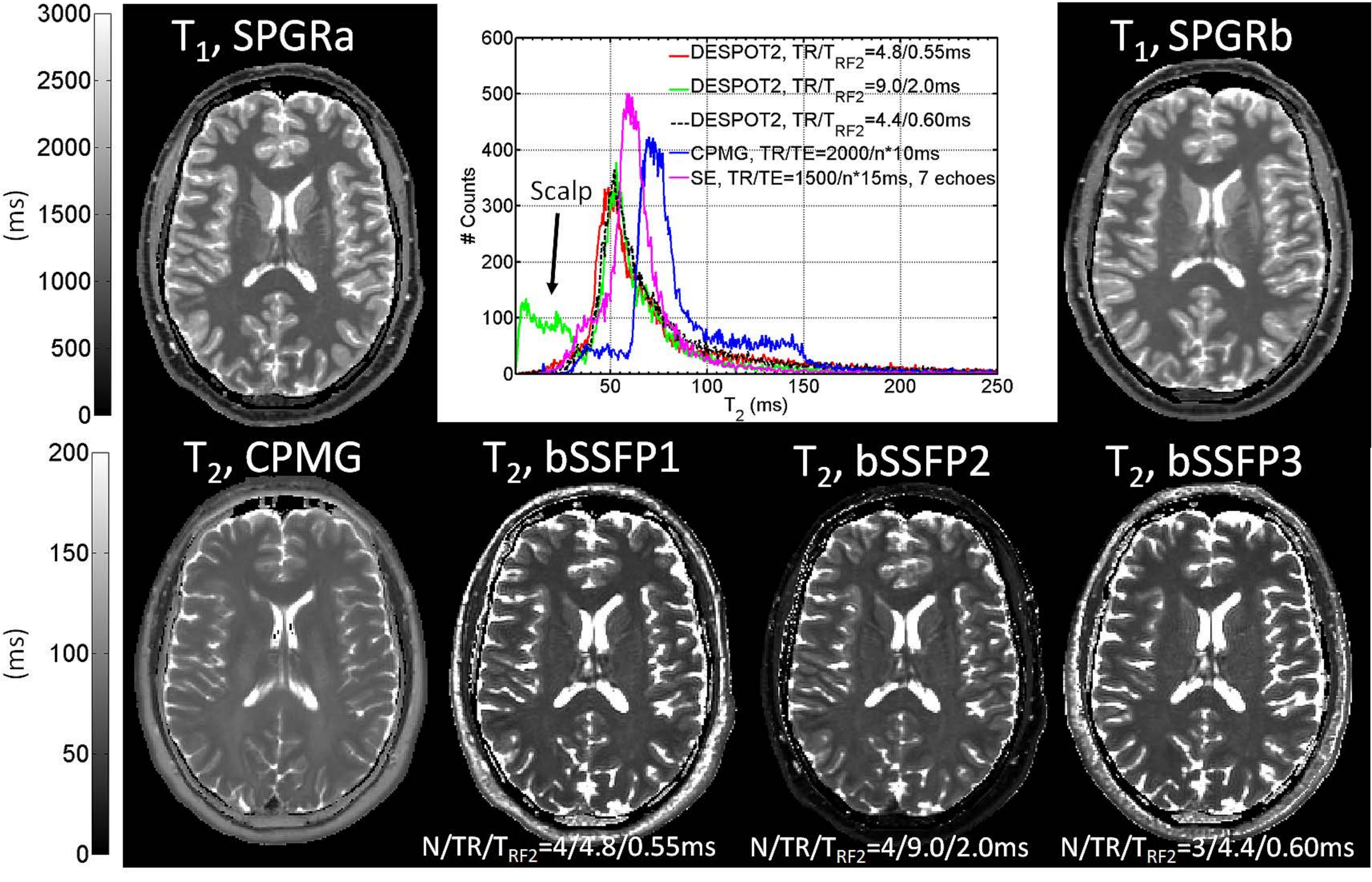
3000
2500
2000
1500
1000
500
0
(ms)
200
150
100
50
0
(ms)
T1, SPGRa
T1, SPGRb
T2, CPMG
T2, bSSFP1
T2, bSSFP2
T2, bSSFP3
DESPOT2, TR/TRF2=4.8/0.55ms
DESPOT2, TR/TRF2=9.0/2.0ms
DESPOT2, TR/TRF2=4.4/0.60ms
CPMG, TR/TE=2000/n*10ms
SE, TR/TE=1500/n*15ms, 7 echoes
Scalp
Counts
T2 (ms)
600
500
400
300
200
100
0
50
100
150
200
250
N/TR/TRF2=4/4.8/0.55ms
N/TR/TRF2=4/9.0/2.0ms
N/TR/TRF2=3/4.4/0.60ms